Metallogeny of the Lietinggang-Leqingla Fe–Cu–(Mo)–Pb–Zn polymetallic deposit, evidence from Geochronology, Petrogenesis, and Magmatic oxidation state, Lhasa terrane

Ai-ping Zhang[a], Yuan-chuan Zheng[b,*], Bo Xu[b], Qiang Fu[c], Wang Ma[b], Chang-da Wu[b], Chi Zhang[b], Yang Shen[b], Fan Fei[c]

[a] School of Resources, Environment and Earth Sciences, Yunnan University, Kunming 650500, PR China
[b] State Key Laboratory of Geological Processes and Mineral Resources, and School of Earth Sciences and Resources, China University of Geosciences, Beijing 100083, PR China
[c] Institute of Geology, Chinese Academy of Geological Sciences, Beijing 100037, PR China

ARTICLE INFO

ABSTRACT

Lietinggang-Leqingla deposit consists of Lietinggang Fe–Cu–(Mo) ore block and Leqingla Pb–Zn–(Fe–Cu) ore block, locating in the southern margin of the central Lhasa subterrane. The ore occurs as laminated or lenticular units in skarns, distributed in the contact zone between the Jubuzhari complex intrusions and carbonate strata of the Mengla Formation. Intrusions associated with the two ore blocks are granodiorite, granodiorite porphyry, and granite porphyry of 62.4 ± 1.2 Ma, 62.6 ± 0.6 Ma, and 63.7 ± 1.0 Ma by zircon U–Pb age dating. Molybdenite Re–Os analyses yield an isochron age of 59.0 ± 1.7 Ma, with a MSWD of 1.6. Comparable isotopic ages between the intrusions and mineralization indicate that they are genetically related, and occurred during or shortly before the main stage of the Indian–Asian continental collision. Granodiorites have SiO_2 content of 62.0–69.1 wt%; Al_2O_3 content of 15.1–15.3 wt%; total alkali concentration ($K_2O + Na_2O$) of 6.63–7.46 wt% and vary in terms of the differentiation index (DI = 67–78). Rocks from the granodiorite porphyry and granite porphyry are characterized by high SiO_2 contents (72.3–74.0 wt%; 74.8–75.8 wt%) and DI (89–90; 93–94). Contents of CaO, Al_2O_3, MgO, Fe_2O_3, P_2O_5, TiO_2 of granodiorite, granodiorite porphyry and granite porphyry show negative correlations with SiO_2. Samples from the granite porphyry have the most negative Eu anomalies (δEu = 0.35–0.36), which are lower than the granodiorite porphyry and granodiorite (δEu = 0.46–0.55 and 0.46–0.66). All the rocks are enriched in large-ion lithophile elements (Rb, Ba, Pb, K and Th) and depleted in high-field-strength elements (Ta, Ti and Nb). The granodiorites have zircon $\epsilon_{Hf(t)}$ values from $+2.5$ to $+8.4$, while $\epsilon_{Hf(t)}$ values of the granodiorite porphyries and granite porphyries range from -6.3 to $+6.8$, and $+1.8$ to $+6.9$, respectively. These data suggest that the three types of intrusions are genetically related, and the less evolved granodiorites are I-type granites that were derived from a mantle-crust mixed source. The granodiorite porphyries and granite porphyries were strongly fractionated, and most likely derived from the melts represented by granodiorites through fractional crystallization of plagioclase, hornblende, biotite, ilmenite, titanite, apatite, and zircon. Zircon trace elements (average ΔFMQ values of granodiorites, granodiorite porphyries, granite porphyries are 0.15, -0.07 and 0.25, respectively) indicate that the Lietinggang-Leqingla magmas were weakly oxidized to moderately reduced. The involvement of mantle materials and medium oxygen fugacity controlled the Fe-Cu mineralization, while the contribution of ancient crustal end-member and strongly fractional crystallization caused the Pb–Zn mineralization of the Lietinggang-Leqingla deposit. Combined with previously published data, we suggest that the Fe–Cu–Pb–Zn fertilities of magmas in the central Lhasa subterrane and their metal series were not only influenced by magma sources, but also by the evolution degree (fractional crystallization) and oxidation state of the magmas.

* Corresponding author at: State Key Laboratory of Geological Processes and Mineral Resources, School of Earth Sciences and Resources, China University of Geosciences, 29# Xueyuan Road, Haidian District, Beijing 100083, PR China.
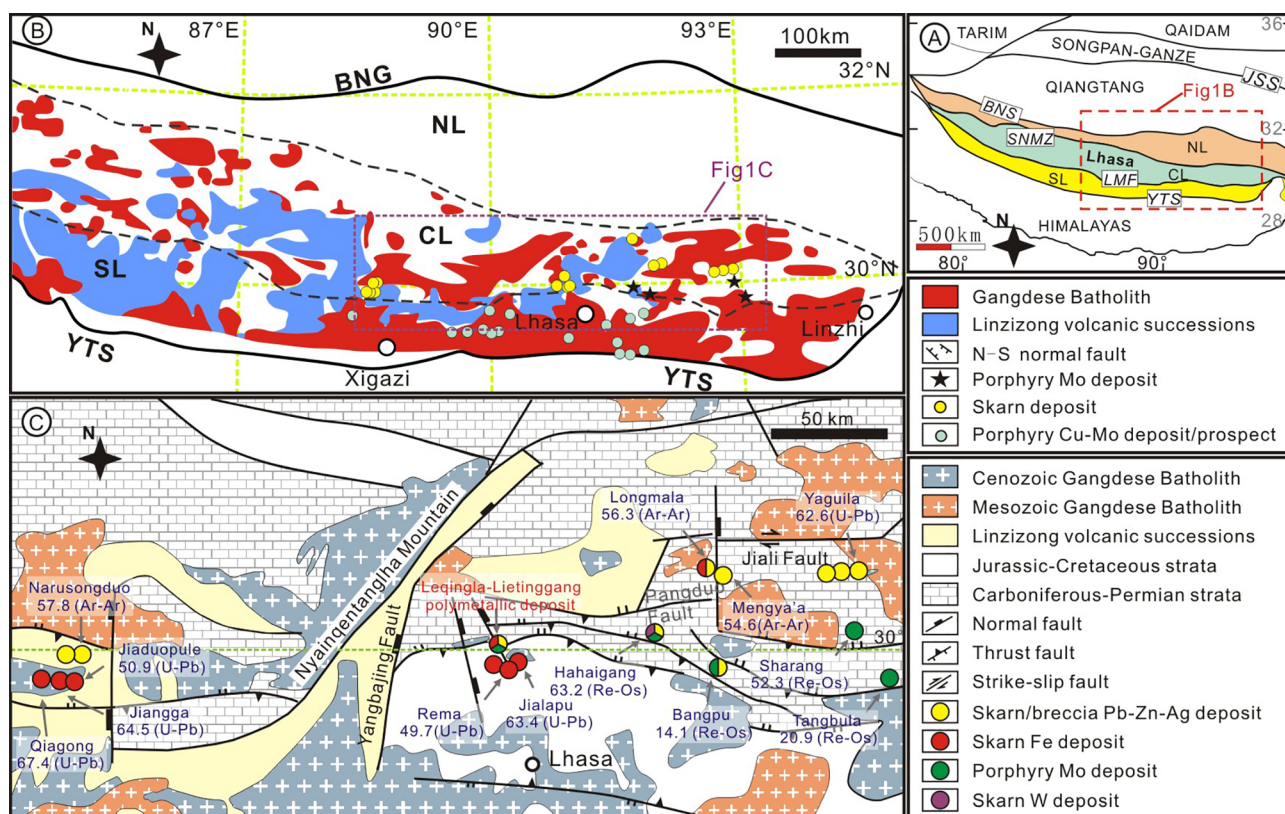*E-mail address:* zhengyuanchuan@gmail.com (Y.-c. Zheng).

Fig. 1. A) Geological sketch map of Tibetan Plateau, modified from Zhu et al. (2011); B) Simplified regional geological map and distribution of deposits in Gangdese belt, modified from Zhu et al. (2011) and Zheng et al. (2015); C) Simplified regional geological map of northern Gangdese belt with Fe–Cu, Pb–Zn–(Ag), Mo and polymetallic deposits formed during different episodes, modified from Zheng et al. (2015). The references for the geochronologic data are listed in the text. Abbreviations: BNS–Banggong–Nujiang suture zone; CL–Central Lhasa subterrane; JSS–Jinshajiang suture zone; LMF–Luobadui–Mila Mountain Fault; NL–Northern Lhasa subterrane; SL–Southern Lhasa subterrane; SNMZ–Shiquan River–Nam Tso ophiolite mélange zone; YTS–Yarlung-Tsangpo suture zone.

1. Introduction

The genetic association between magmas and hydrothermal ore deposits was well documented in scores of geological studies of mineralization close to magmatic intrusions (Titley and Beane, 1981; Sillitoe, 1989; Hedenquist and Lowenstern, 1994; Meinert, 1992; Sillitoe, 2010). A large amount of attention has been paid to the influences of the nature of associated magmas, such as magmatic oxidation condition, water content, and magmatic evolution (Richards and Kerrich, 2007; Chiaradia, 2009; Yang et al., 2015; Hou et al., 2015a,b; Wang et al., 2014a–c, 2018; Zheng et al., 2019), as well as the roles of mantle and crust in magma petrogenesis for the formation of these hydrothermal ore deposits (Deng et al., 2014, 2018; Mao et al., 2011; Richards, 2009, 2011; Wang et al., 2015; Yang et al., 2016; Zheng et al., 2015). The Lhasa terrane is a critical tectonic unit of the Himalayan–Tibetan Orogen (e.g. Mo et al., 2005; Zhu et al., 2011), in which uniqueness and large-scale metallogenesis has drawn plenty of attentions. The metallogenesis was associated with the Mesozoic accretionary orogeny related to subduction of Neo–Tethyan oceanic lithosphere (e.g. Zhu et al., 2009, 2011; Hou et al., 2015b) and the Cenozoic orogeny resulting from the Indian–Asian continental collision (Ding et al., 2017; Hou et al., 2006a; 2006b; 2006c; Hu et al., 2015; Leech et al., 2005; Zhang et al., 2014; Zhu et al., 2015). The mineralization is dominated by the Gangdese porphyry Cu–(Mo–Au) belt (e.g. Xiongcun, Qulong, Jiama, and Zhunuo) and northern Gangdese Pb–Zn–(Ag) belt (e.g. Mengya'a, Yaguila, and Narusongduo). Cu–(Mo–Au) mineralization mainly distributed in the southern Lhasa subterrane, whereas Pb–Zn–(Ag) mineralization spread in the central Lhasa subterrane (Hou et al., 2015a; Zheng et al., 2015).

Previous studies suggested that the Cu–(Mo–Au) mineralization is

mainly controlled by parental magmas characterized by hydrous, sulfur-rich, and high oxygen fugacity, which were derived from a metasomatized mantle wedge or a thickened juvenile lower crust (Hou et al., 2015b; Wang et al., 2014c; Yang et al., 2015), while the Pb–Zn–(Ag) mineralization is associated with S-type granites with low oxygen fugacity, generated from partial melting of ancient crustal materials (Zheng et al., 2015). Recent years, several large deposits contain polymetallic mineralization in the central Lhasa subterrane have been found, such as the Bangpu porphyry-skarn Mo–(Cu)–Pb–Zn deposit (Zhao et al., 2015), Hahaiguang skarn W–Mo–(Cu–Pb–Zn) (Li et al., 2014), Longmala skarn Fe–(Cu)–Pb–Zn deposit (Fu et al., 2012, 2014), and Lietinggang-Leqingla skarn Fe–Cu–(Mo)–Pb–Zn deposit (Ma et al., 2015). Compared to the Gangdese porphyry Cu–(Mo–Au) deposits and the north Gangdese Pb–Zn–(Ag) deposits, the polymetallic mineralization in the Lhasa terrane has not been well studied. Consequently, the key factors controlling the intensity of these polymetallic deposits, especially the nature of associated magmas, including the magma sources, evolution degrees and magmatic oxidation states, were not well constrained in the central Lhasa subterrane.

Lietinggang-Leqingla is one of the typical polymetallic deposits in the Lhasa terrane, which contains both Fe–Cu–(Mo) and Pb–Zn mineralization. Here, we describe the geology and geochronology of this deposit, which indicate that the Fe–Cu–(Mo)–Pb–Zn mineralization are genetically associated with the Jubuzhari felsic complex, and then discuss the petrogenesis of the associated intrusions by geochemical data. Zircon trace elements data are used to constrain on magmatic oxidation of the ore-forming intrusions. Our data indicate that magma source, magmatic oxidation, and magmatic fractional crystallization degree are the key factors determining the metallogenesis of the Lietinggang-Leqingla Fe–Cu–Pb–Zn polymetallic mineralization.

Moreover, the evolution of the Fe–Cu–Pb–Zn mineralization in the Lhasa Terrane is concluded combined with previously published data.

2. Regional setting

2.1. Tectonic setting

The Himalayan–Tibetan Plateau is composed of four tectonic blocks, including the Himalayan, Lhasa, Qiangtang, and Songpan–Ganze blocks, from south to north (Yin and Harrison, 2000; Chung et al., 2005) (Fig. 1A). The Lhasa terrane is bounded to the north by the Bangong–Nujiang suture, formed by the closure of the Bangong–Nujiang Ocean and collision between the Lhasa and Qiangtang terranes during the Late Jurassic to the Early Cretaceous (Yin and Harrison, 2000; Zhu et al., 2009, 2012) (Fig. 1B). It can be further subdivided into northern, central, and southern subterranes, which are separated by the Shiquanhe–Nam Tso Mélange Fault and Luobadui–Milashan Fault, respectively (Pan et al., 2004, 2006; Zhu et al., 2011). This terrane is characterized by Cenozoic E–W-trending thrust systems developed within the central subterrane and N–S-striking normal fault systems across the entire terrane (Fig. 1C). A southward-thrusting event formed thin-skinned structures and led to widespread exposure of Ordovician–Triassic strata and Mesozoic granitoid batholiths in the central Lhasa subterrane (Wu et al., 2003b). N–S-striking normal faults produced by mid-Miocene east–west crustal extension (Coleman and Hodges, 1995; Blisniuk et al., 2001) (Fig. 1B).

2.2. Stratigraphy and magmatism

The Lhasa terrane comprises Precambrian crystalline basement, Paleozoic to Mesozoic sedimentary and volcanic rocks, and Mesozoic to Cenozoic volcanic and plutonic rocks (Pan et al., 2006; Zhu et al., 2012; Zheng et al., 2012a,b, 2014, 2016). The Precambrian crystalline basement along the northern margin of the terrane mainly comprises orthogneiss (e.g. Amdo orthogneiss) (Guynn et al., 2006). The widespread cover successions are Permian–Carboniferous arc volcanic rocks and abundant glaciomarine diamictites, Cambrian volcanic rocks, Upper Jurassic to Lower Cretaceous sedimentary rocks intercalated with abundant volcanic rocks, and minor amounts of Ordovician, Silurian, Devonian, and Triassic marine clastic sedimentary rocks (Harris et al., 1988; Pan et al., 2004; 2012; Ji et al., 2009).

A complex magmatic history is characterized by the Lhasa terrane since the Jurassic. Prior to Indian–Asian continental collision, the Lhasa terrane was affected by Jurassic subduction of the Neo-Tethyan oceanic slab, produced the Xigaze forearc basin (Dürr, 1996; Ji et al., 2009) and Andean-type Gangdese magmatic arc batholiths (Chu et al., 2006; Wang et al., 2008). The Indian–Asian continental collision began in the Cenozoic and throughout this protracted and varied tectonic event, emplacement of voluminous arc batholiths and eruption of widespread Linzizong volcanic successions took place across a vast region of the southern Tibet (Fig. 1A, B) (Mo et al., 2005, 2007; Zhu et al., 2009, 2011, 2015). The arc batholiths include the Paleocene *syn*-collisional granitoids, Eocene gabbros and associated granitoid intrusions, and basaltic subvolcanic rocks (Hou and Cook, 2009). The Linzizong volcanic successions are calc-alkaline and high-K calc-alkaline with minor shoshonitic andesitic-rhyolitic compositions, and yield a wide range of ages, varying from 69 to 61 Ma (Dianzhong unit), 61–54 Ma (Nianbo unit), and 54–44 Ma (Pana unit) (Zhu et al., 2015). Miocene magmatism in the Lhasa terrane was characterized by potassic-ultrapotassic volcanic rocks (Ding et al., 2003; Zhao et al., 2006; Xu et al., 2017), and adakitic intrusive rocks (Hou et al., 2015; Yang et al., 2016; Zheng et al., 2012a,b, 2014).

2.3. Mineralization

Several types of ore deposits were recognized in the Lhasa terrane:

porphyry Cu–(Mo–Au), porphyry Mo, skarn Fe–(Cu), granite-related Pb–Zn–(Ag) and porphyry-skarn polymetallic deposits since the Indian–Asian continental collision (Hou and Cook, 2009; Hou et al., 2015b; Zheng et al., 2015). Porphyry Cu–(Mo–Au) deposits, the most economically resources in the Himalayan–Tibetan orogen, are mainly formed in the Miocene distributed in the southern subterrane (Fig. 1B). Porphyry Mo deposits formed in the central Lhasa subterrane, represented by the Sharang (52.3 Ma, Zhao et al., 2014), and Tangbula (20.9 Ma, Wang et al., 2010) (Fig. 1B, C). The skarn Fe–(Cu) deposits, formed from 65 Ma to 49 Ma, are regarded associated with *syn*-collisional metaluminous granodiorites at the southernmost margin of the central Lhasa subterrane (Fu et al., 2013; Zheng et al., 2015) (Fig. 1B, C). The granite-related Pb–Zn–(Ag) deposits, formed during 65–55 Ma, have huge economical potential (~100 Mt of Pb + Zn ore resources with several large-scale deposits, including the Mengya'a, Yaguila, and Narusongduo), most of which are located in northern margin of the central Lhasa subterrane. Three types of granite-related Pb–Zn–(Ag) mineralization have been recognized, including skarn hosted, breccia hosted, and porphyry-like hosted (Fu et al., 2015, 2017; Gao et al., 2011; Huang et al., 2012; Ji et al., 2012b; Zheng et al., 2015). The polymetallic deposits are distributed in the central Lhasa subterrane including Bangpu porphyry-skarn Mo–(Cu)–Pb–Zn deposit (15 Ma, Zhao et al., 2015), Hahaiguang skarn W–Mo–(Cu–Pb–Zn) (63 Ma, Li et al., 2014), Longmala skarn Fe–(Cu)–Pb–Zn deposit (56 Ma, Fu et al., 2014) and Lietinggang-Leqingla skarn Fe–Cu–(Mo)–Pb–Zn deposit. The skarn Fe–(Cu), granite-related Pb–Zn–(Ag), porphyry Mo and these polymetallic deposits distributed in the central Lhasa subterrane composed the northeastern Gangdese Pb–Zn–Ag–Fe–Mo–W polymetallic belt (NGPB) (Zheng et al., 2015). In particular, the Lietinggang-Leqingla is one of the typical polymetallic deposits in the NGPB.

3. Geology of the Lietinggang-Leqingla deposit

TheLietinggang–Leqingla Fe–Cu–(Mo)–Pb–Zn deposit is located in the southern margin of the central Lhasa subterrane (30°01′-30°04′N, 90°57′-91°01′E) (Fig. 1C, 2). It holds 15 Mt Fe ore, 0.5 Mt Cu ore, more than 7 Mt of Pb + Zn ore, with average grades of 55.27 wt% Fe, 1.07 wt % Cu, and 7.74 wt% Pb + Zn, respectively. Sedimentary rocks in the mining district are the middle Permian Luobadui Formation, the upper Permian Mengla Formation, the Upper Triassic Jialapu Formation, and the Eocene–Quaternary Nianbo Formation. The Luobadui Formation is characterized by tuffaceous sandstone, thick limestone, and andesite and basalt from south to north, while the Mengla Formation is dominated by tuffaceous sandstone, limestone and slate, and calcilutite, siltstone. The Upper Triassic Jialapu Formation is mainly composed of sandstone, siltstone, and mudstone, and the Nianbo Formation is pyroclastic rock (Fig. 2). In addition, Quaternary alluvium covers areas in the south and north of the mine district (Fig. 2).

The Lietinggang-Leqingla deposit consists of Lietinggang Fe–Cu–(Mo) ore block and Leqingla Pb–Zn–(Fe–Cu) ore block. All the orebodies occurr in skarns, distributed in the contact zone between the Jubuzhari complex and carbonate strata of the Mengla Formation. The Lietinggang and Leqingla ore blocks occur on the north and southwest boundaries of the complex.

3.1. Orebodies

In the Lietinggang Fe–Cu–(Mo) ore block, the orebodies are characterized by laminated or lens-shaped units occurred in the garnet-pyroxene skarns, which distributed in the carbonate strata of the Mengla Formation, about 50 m–200 m from the northern edge of the complex (Fig. 3A).

The Leqingla Pb–Zn–(Fe–Cu) orebodies are developed as layered or lens-shaped units in the garnet-pyroxene skarns, pyroxene-actinolite skarns and epidote-chlorite skarns. The garnet-pyroxene skarns are located in the contact zone between the Jubuzhari complex and marble of
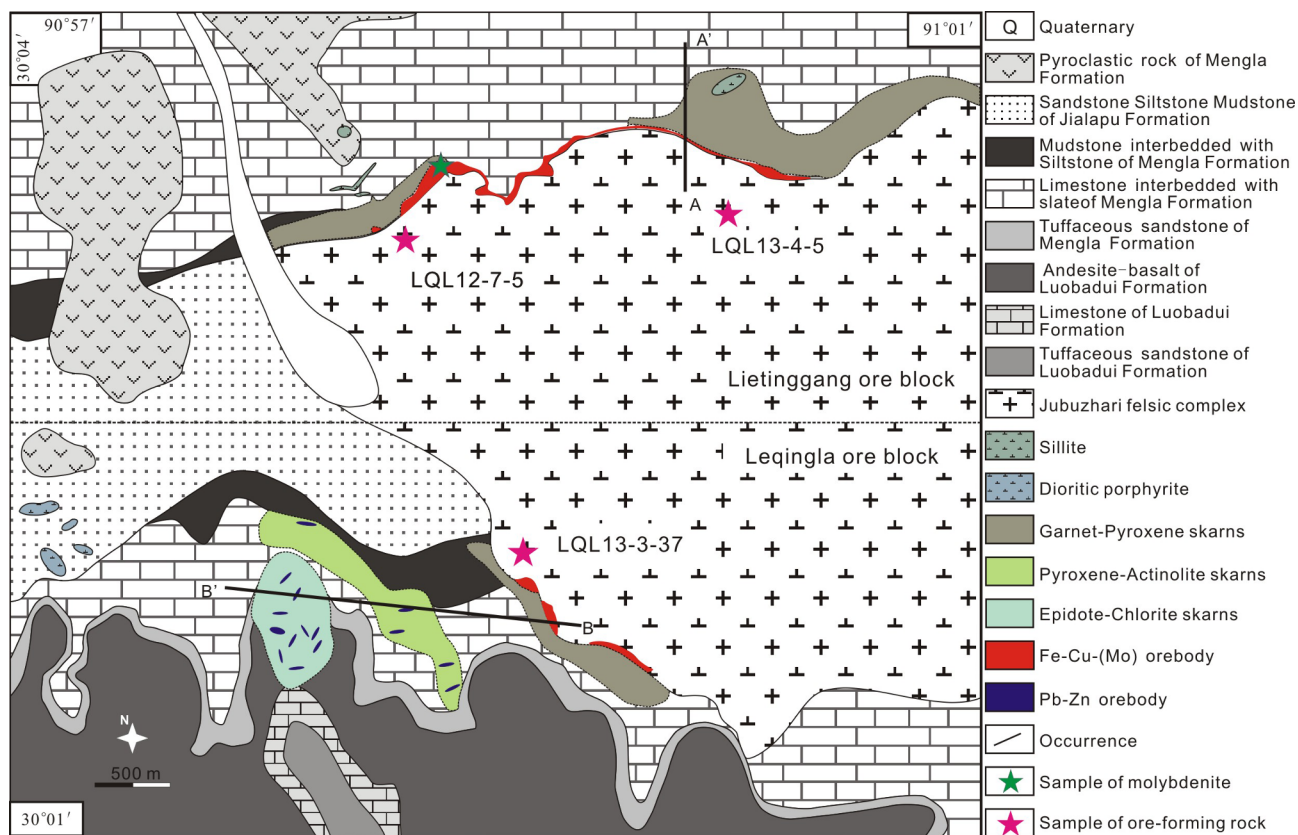
Fig. 2. Geological map of the Lietinggang-Leqingla Fe–Cu–(Mo)–Pb–Zn deposit, modified from Ma et al. (2015).

the Mengla Formation, in which most Fe–Cu orebodies are developed (Fig. 3B). The pyroxene-actinolite skarns develop in the carbonate strata of the Mengla Formation about 700 m–1000 m from the western edge of the complex. The epidote-chlorite skarns, which occur in carbonate strata of the Mengla Formation, locate at about 1.5 km–1.8 km from the western edge of the complex. The Pb–Zn orebodies are mainly hosted by both the the pyroxene-actinolite skarns and epidote-chlorite skarns (Fig. 3B).

Fig. 3. A) Geological profile of A–A′ showing the zones of alteration and mineralization of the Fe–Cu–(Mo) orebodies in the Lietinggang ore block; B) Geological profile of B–B′ showing the zones of alteration and mineralization of the Pb–Zn–(Fe–Cu) orebodies in the Leqingla ore block.
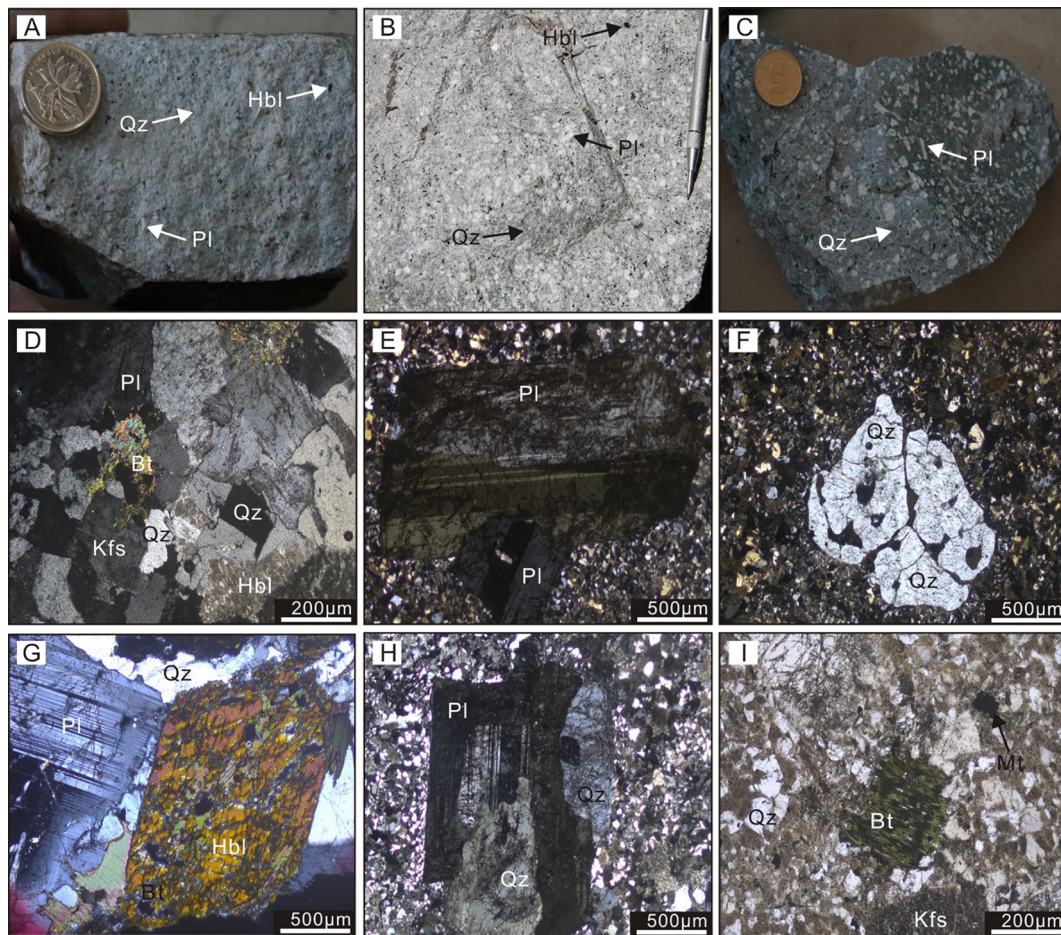
Fig. 4. Petrographical and photomicrograph of the Jubuzhari complex intrusions in the Lietinggang-Leqingla deposit. A) The granodiorite is massive and coarse-grained in texture, and mainly contains quartz, plagioclase and hornblende; B) The porphyritic granodiorite porphyry contains phenocrysts of quartz, plagioclase and hornblende; C) The porphyritic granite porphyry contains phenocrysts of quartz and plagioclase; D) The granodiorite is mainly composed of quartz, plagioclase, K-feldspar, and a small amount of hornblende and biotite; E-G) The phenocrysts of plagioclase, quartz, and hornblende e in the granodiorite porphyry; H) The phenocrysts of plagioclase and quartz in the granite porphyry; I) The phenocrysts of K-feldspar, quartz and biotite (suffered from chloritization) in the granite porphyry, with minor magnetite. Abbreviations: Hbl–Hornblende; Bt–Biotite; Kfs–K-feldspar; Mt–Magnetite; Pl–Plagioclase; Qz–Quart.

3.2. Magmatism

The Jubuzhari felsic complex is exposed over a large area, emplacing as stock and dikes in the southeast of the mine district (Fig. 2). The complex is mainly composed of granodiorite, granodiorite porphyry and granite porphyry (Fig. 4A–C), and granodiorite gradually transitions to granodiorite porphyry through granodiorite porphyry from center to edge of the complex. The granodiorite is massive and coarse-grained in texture (Fig. 4A), and contains mainly of plagioclase (~35 vol%), quartz (~30 vol%), K-feldspar (~15 vol%), and biotite and hornblende (15–20 vol%) (Fig. 4D), with minor accessory minerals (apatite and magnetite). The granodiorite porphyry is porphyritic in texture (Fig. 4B), and contains phenocrysts of plagioclase (~30 vol%) (Fig. 4E), quartz (~35 vol%) (Fig. 4F) K-feldspar (~15 vol%) and hornblende (~15 vol%) (Fig. 4G), set in a fine-grained groundmass of quartz, plagioclase, and minor biotite and hornblende. The granite porphyry is also porphyritic in texture (Fig. 4C). The phenocrysts are mainly composed of plagioclase (25 vol%), quartz (40 vol%) andK-feldspar (~20 vol%) (Fig. 4H–I). The groundmass are quartz, plagioclase, biotite, and magnetite (Fig. 4I). Small-scaled sillite and dioritic porphyrite stocks were intruded into the limestone of Mengla Formation and sandstone, siltstone, and mudstone of the Jialapu Formation, respectively (Fig. 2).
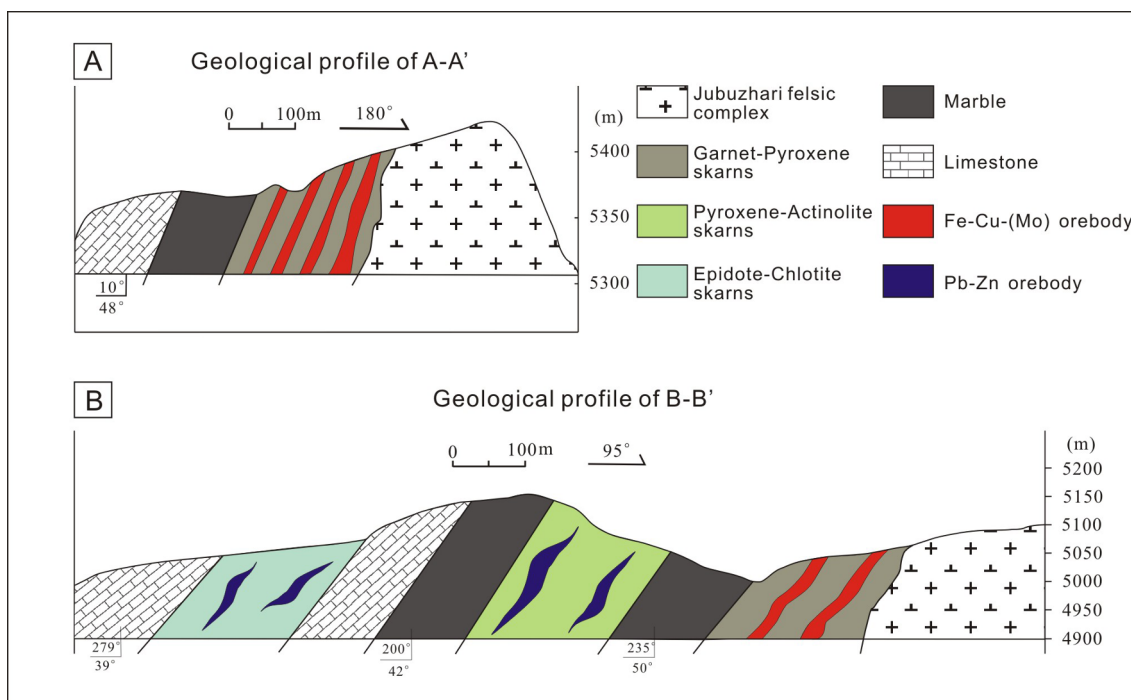
3.3. Mineralization and alteration

Ore minerals in the Lietinggang Fe–Cu–(Mo) ore block are magnetite, chalcopyrite, pyrrhotite, and molybdenite, occurred as massive or disseminated form in the skarns (Fig. 5A, B). Euhedral to subhedral magnetite and pyrrhotite grains are surrounded and replaced by chalcopyrite in a massive magnetite-dominant ore (Fig. 5E). In the disseminated ore, molybdenite and chalcopyrite show a paragenesis relationship infilled the spaces between garnet crystals (Fig. 5F). In the Leqingla Pb–Zn–(Fe–Cu) ore block, ore minerals are sphalerite, galena, chalcopyrite, magnetite, and pyrrhotite in decreasing order of abundance. The ore minerals occur as massive or disseminated form in the skarns (Fig. 5C, D). Chalcopyrite is exsolved as emulsion in the massive sphalerite and galena ore (Fig. 5G). In the disseminated ore, sphalerite, galena, and chalcopyrite, show a paragenesis relationship with epidote (Fig. 5H).

In the mining area, the alteration is usually related to skarn formation. There are three major types of skarns in the Lietinggang-Leqingla deposit, which are the garnet-pyroxene skarns, pyroxene-actinolite skarns and epidote-chlorite skarns. In general, the garnet-pyroxene skarns, which have a close relationship with the Fe–Cu–(Mo) mineralization and distributed close to the Jubuzhari complex, are mainly composed of coarse-grained garnet, hedenbergite, and diopside
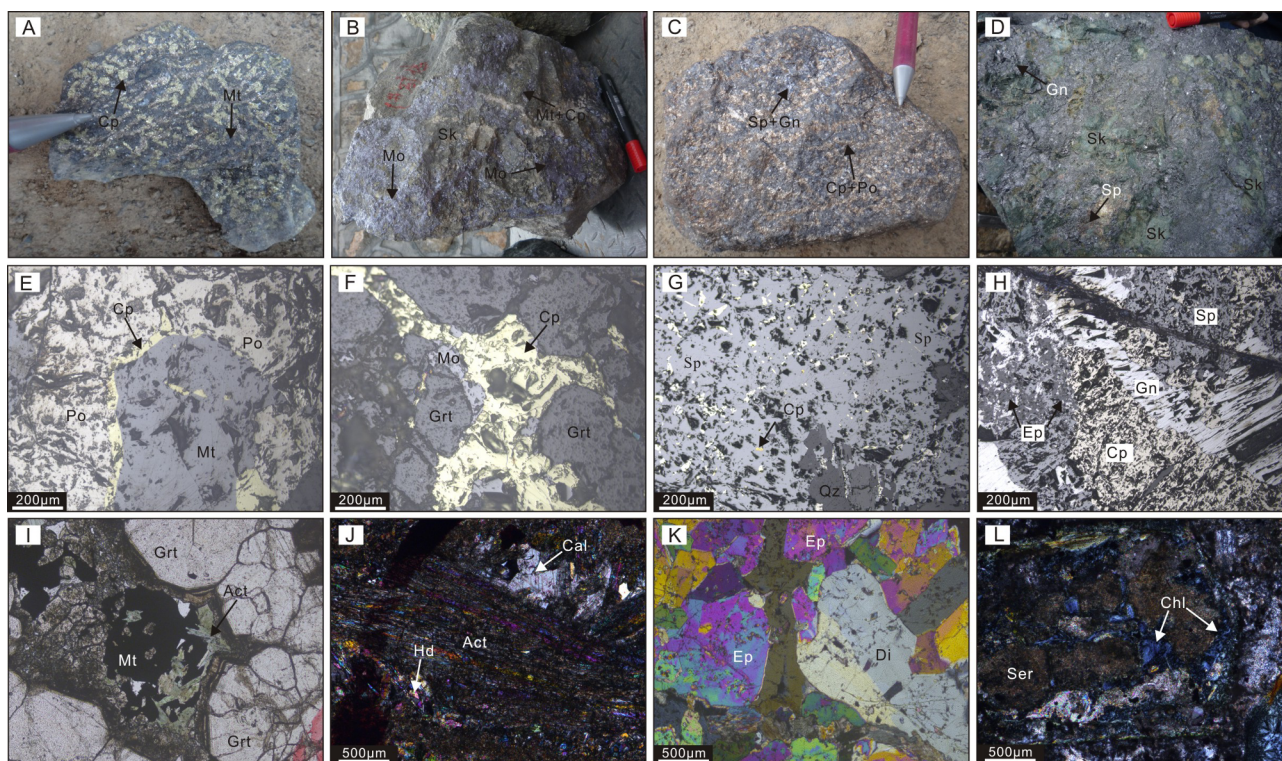
Fig. 5. Petrographical and photomicrograph of Fe–Cu–(Mo)–Pb–Zn mineralization and alteration in the Lietinggang-Leqingla deposit. A) Massive magnetite and chalcopyrite ore from the Lietinggang ore block; B) Disseminated molybdenite, magnetite and chalcopyrite in skarn from the Lietinggang ore block; C) Massive sphalerite, galena, chalcopyrite, and phrrhotite ore from the Leqingla ore block; D) Disseminated galena and sphalerite in skarn from the Leqingla ore block; E) Euhedral to subhedral magnetite and pyrrhotite is surrounded and replaced by chalcopyrite in the massive ore from the Lietinggang ore block; F) Molybdenite and chalcopyrite show a paragenesis relationship infilled the spaces between garnet crystals in the Lietinggang ore block; G) Chalcopyrite is exsolved as emulsion in the massive sphalerite and galena ore from the Leqingla ore block; H) Sphalerite, galena, and chalcopyrite showing a paragenesis relationship with epidote in the disseminated ore from Leqingla ore block; I) Garnet in skarn, with magnetite and actinolite infilling the spaces between garnet crystals; J) Hedenbergite and actinolite in skarn; K) Diopside and epidote in skarn; L) Sericite and chlorite in skarn. Abbreviations: Act–Actinolite; Cal–Calcite; Chl–Chlorite; Cp–Chalcopyrite; Di–Diopside; Ep–Epidote; Gn–Galena; Grt–Garnet; Hd–Hedenbergite; Mo–Molybdenite; Mt–Magnetite; Po–Phrrhotite; Qz–Quartz; Ser–Sericite; Sk–Skarn; Sp–Sphalerite.

(Fig. 5I). The pyroxene-actinolite skarns comprise hedenbergite and actinolite (Fig. 5J), while the epidote-chlorite skarns consist of epidote, chlorite and minor sericite (Fig. 5K, L). Most of the Pb–Zn orebodies are hosted by the pyroxene-actinolite and epidote-chlorite skarns that located far away from the complex.

According to the skarn mineral assemblage relationships, five stages of alteration–mineralization resulted in the formation of the skarn orebodies in the Lietinggang-Leqingla deposit: prograde skarn stage → oxides stage → retrograde skarn stage → quartz–sulfide stage → carbonate stage. The prograde skarn stage is characterized by the formation of garnet, diopside and actinolite. In the oxides stage, the main mineral is magnetite, which assembled the Fe orebodies. The retrograde skarn stage resulted in the formation of massive actinolite, epidote, chlorite, and minor quartz and calcite. The quartz–sulfide stage is responsible for the formation of the bulk of the Pb-Zn orebodies, and is mineralogically dominated by sphalerite, galena, chalcopyrite, and abundant quartz and calcite. The carbonate stage is characterized by the formation of chlorite + sericite + quartz + pyrite + calcite.

4. Descriptions of analytical methods

4.1. LA–ICP–MS U–Pb dating and trace elements

In this study, three samples (LQL13-4-5, LQL12-7-15, and LQL13-3-37) were chosen for zircon U–Pb dating and rare earth elements (REE) analyses. Zircon grains were separated by standard density and magnetic techniques before finally hand-picked under a binocular microscope, and then mounted on an epoxy resin and polished down to approximately half section to expose the grain centers. Prior to analytical work, all zircon grains were examined under a microscope with transmitted and reflected light as well as cathode luminescence (CL) images using a scanning electron microscope (CL-SEM) to reveal their internal structures (Fig. 6A, C, E).

Zircon U–Pb dating and rare earth elements (REE) analyses were conducted using laser ablation inductively coupled plasma mass spectrometry (LA–ICP–MS) at the Geologic Lab Centre, China University of Geosciences (Beijing). The instrument couples a quadrupole ICP-MS (Agilient 7500a) and a UP-193 Solid-State laser (193 nm, New Wave Research Inc.) with the automatic positioning system. For the present work, laser spot size was set to ∼36 μm, laser energy density at 8.5 J/cm^2 and repetition rate at 10 Hz. The procedure of laser sampling is 5 s pre-ablation, 20 s sample-chamber flushing and 40-s sampling ablation. The ablated material is carried into the ICP-MS by the high-purity Helium gas stream with flux of 0.8 L/min. The whole laser path was fluxed with N$_2$ (15 L/min) and Ar (1.15 L/min) in order to increase energy stability. The counting time for U, Th, ^{204}Pb, ^{206}Pb, ^{207}Pb and ^{208}Pb is 20 ms, and is 15 ms for other elements. Calibrations for the zircon analyses were carried out using NIST 610 glass as an external standard and Si as internal standard. U–Pb isotope fractionation effects were corrected using zircon 91,500 (1064 Ma) (Wiedenbeck et al., 1995) as external standard. Zircon standard TEMORA (417 Ma) from Australia (Black et al., 2003) is also used as a secondary standard to supervise the deviation of age measurement/calculation. During analytical sessions, the obtained ^{206}Pb/^{238}U of 91,500 and TEMORA are 1063 Ma and 417 Ma, respectively. Isotopic ratios and element concentrations of zircons were calculated using GLITTER (ver. 4.4,
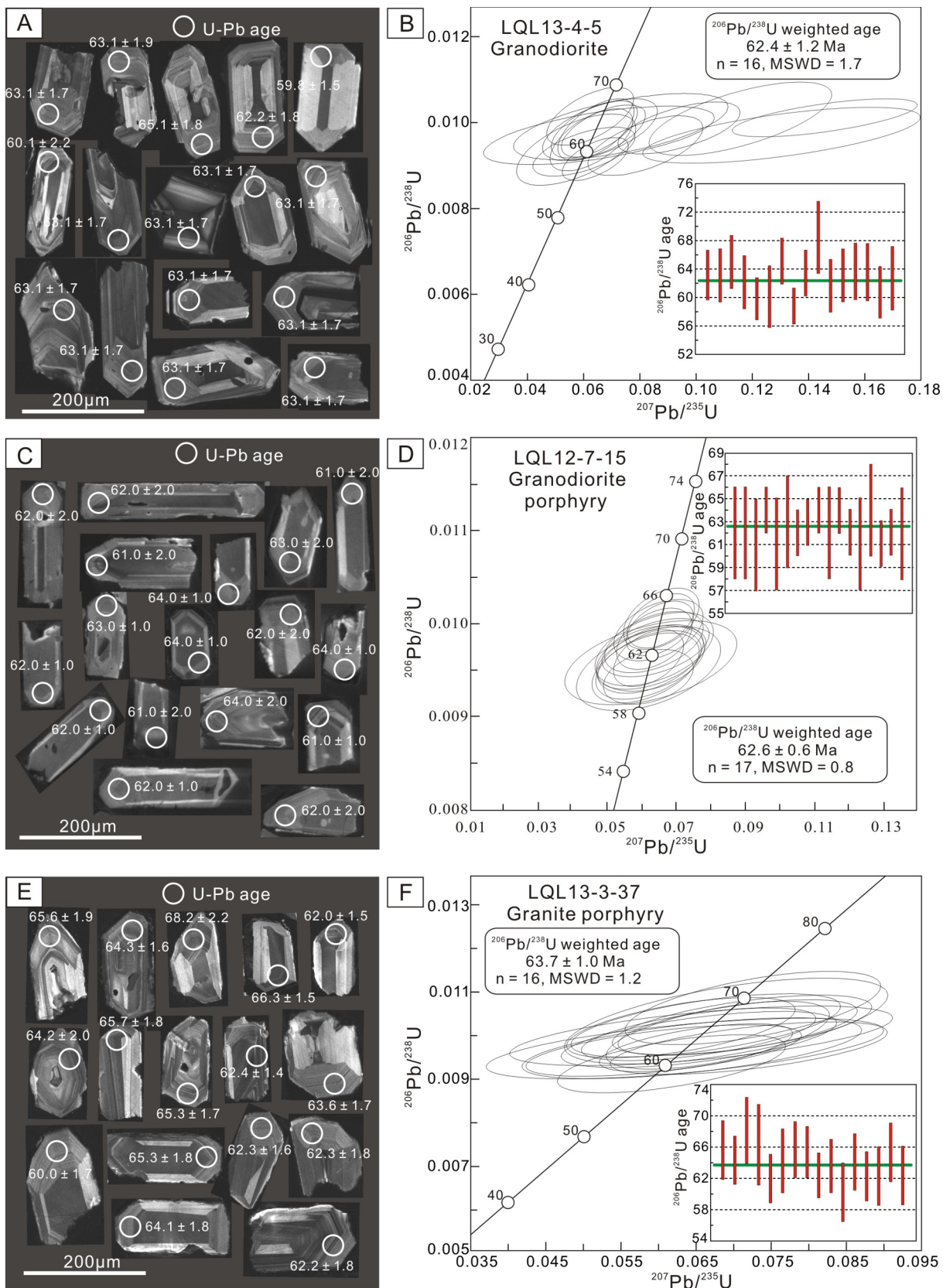
Fig. 6. Analytical zircon CL images (A, C, E) and Zircon U–Pb concordia diagrams (B, D, F) of the granodiorite, granodiorite porphyry, and granite porphyry in the Lietinggang-Leqingla deposit.
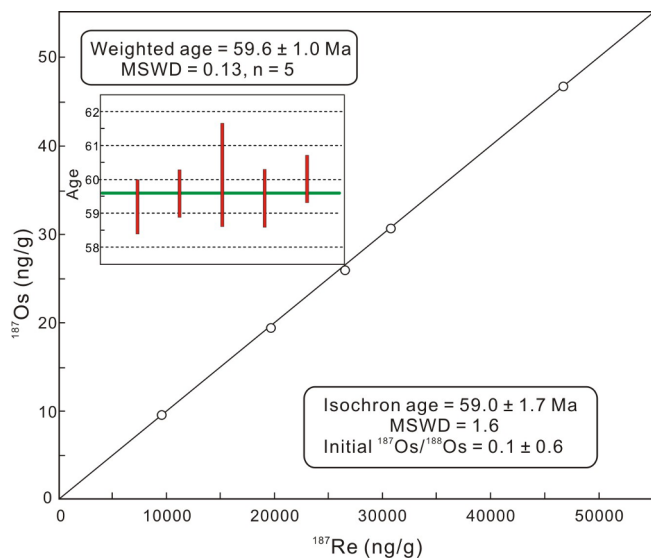
Table 1

LA–ICP–MS zircon U–Pb ages for the granodiorite, granodiorite porphyry, and granite porphyry in the Lietinggang-Leqingla deposit.

Analysis sample	Rock type	Th (ppm)	U (ppm)	Th/U	$^{207}Pb/^{206}Pb$		$^{207}Pb/^{235}U$		$^{206}Pb/^{238}U$		$^{207}Pb/^{235}U$		$^{206}Pb/^{238}U$	
					Ratio	1σ	Ratio	1σ	Ratio	1σ	Age (Ma)	1σ	Age (Ma)	1σ
LQL13-4-5-2	Granodiorite	217	417	0.519928	0.04648	0.00500	0.06383	0.00626	0.00984	0.00027	62.8	6.0	63.1	1.7
LQL13-4-5-3		154	321	0.478482	0.05071	0.00741	0.06583	0.00835	0.00984	0.00029	64.7	8.0	63.1	1.9
LQL13-4-5-5		222	399	0.556248	0.04737	0.00608	0.06233	0.00632	0.01015	0.00028	61.4	6.0	65.1	1.8
LQL13-4-5-6		255	391	0.653107	0.04959	0.00970	0.06547	0.01678	0.00970	0.00028	64.4	16.0	62.2	1.8
LQL13-4-5-7		315	464	0.679106	0.04973	0.00692	0.06014	0.00742	0.00932	0.00023	59.3	7.1	59.8	1.5
LQL13-4-5-8		187	326	0.572443	0.05185	0.00937	0.05737	0.00867	0.00937	0.00034	56.6	8.3	60.1	2.2
LQL13-4-5-9		580	667	0.869610	0.10137	0.00960	0.14896	0.01559	0.01015	0.00025	141.0	13.8	65.1	1.6
LQL13-4-5-10		1169	890	1.314570	0.05182	0.00431	0.06419	0.00480	0.00915	0.00020	63.2	4.6	58.7	1.3
LQL13-4-5-12		281	624	0.450898	0.07036	0.00683	0.09392	0.00888	0.00988	0.00025	91.2	8.2	63.4	1.6
LQL13-4-5-13		97	215	0.453133	0.08853	0.01236	0.11489	0.01437	0.01068	0.00039	110.4	13.1	68.5	2.5
LQL13-4-5-14		163	369	0.442722	0.04986	0.00660	0.06278	0.00602	0.00960	0.00030	61.8	5.7	61.6	1.9
LQL13-4-5-15		203	394	0.516193	0.04859	0.00538	0.06441	0.00554	0.00984	0.00029	63.4	5.3	63.1	1.9
LQL13-4-5-17		240	445	0.538928	0.05141	0.00602	0.06704	0.00611	0.00980	0.00025	65.9	5.8	62.9	1.6
LQL13-4-5-18		234	399	0.584633	0.06064	0.01498	0.07324	0.01559	0.00991	0.00031	71.8	14.7	63.6	2.0
LQL13-4-5-21		462	811	0.568924	0.06139	0.00543	0.08196	0.00836	0.00946	0.00028	80.0	7.8	60.7	1.8
LQL13-4-5-23		160	356	0.449754	0.09369	0.01408	0.14207	0.02527	0.00977	0.00035	134.9	22.5	62.7	2.2
LQL12-7-15-1	Granodiorite porphyry	76	165	0.460573	0.04736	0.00750	0.06315	0.00990	0.00967	0.00024	62.0	9.0	62.0	2.0
LQL12-7-15-2		82	173	0.471345	0.04729	0.00850	0.06352	0.01130	0.00974	0.00027	63.0	11.0	62.0	2.0
LQL12-7-15-3		96	190	0.503788	0.04728	0.00790	0.06241	0.01030	0.00957	0.00024	61.0	10.0	61.0	2.0
LQL12-7-15-4		84	277	0.302248	0.04732	0.04730	0.04732	0.04730	0.04732	0.04732	64.0	7.0	64.0	1.0
LQL12-7-15-5		148	213	0.695273	0.04728	0.01080	0.06204	0.01400	0.00952	0.00027	61.0	13.0	61.0	2.0
LQL12-7-15-6		147	231	0.635855	0.04734	0.00710	0.06391	0.00950	0.00979	0.00024	63.0	9.0	63.0	2.0
LQL12-7-15-7		300	360	0.834620	0.04727	0.00530	0.06294	0.00700	0.00965	0.00019	62.0	7.0	62.0	1.0
LQL12-7-15-8		117	223	0.522928	0.04720	0.00560	0.06406	0.00750	0.00984	0.00021	63.0	7.0	63.0	1.0
LQL12-7-15-9		135	271	0.497305	0.04727	0.00450	0.06539	0.00620	0.01003	0.00020	64.0	6.0	64.0	1.0
LQL12-7-15-10		85	169	0.505252	0.04734	0.01250	0.06261	0.01640	0.00959	0.00030	62.0	16.0	62.0	2.0
LQL12-7-15-11		252	410	0.613021	0.04738	0.00480	0.06495	0.00660	0.00994	0.00020	64.0	6.0	64.0	1.0
LQL12-7-15-12		93	219	0.425841	0.04735	0.00730	0.06353	0.00980	0.00973	0.00024	63.0	9.0	62.0	1.0
LQL12-7-15-13		72	162	0.446721	0.04718	0.00810	0.06202	0.01060	0.00953	0.00025	61.0	10.0	61.0	2.0
LQL12-7-15-14		97	182	0.531939	0.04718	0.00630	0.06466	0.00860	0.00994	0.00024	64.0	8.0	64.0	2.0
LQL12-7-15-15		179	255	0.701045	0.04726	0.00640	0.06149	0.00820	0.00944	0.00019	61.0	8.0	61.0	1.0
LQL12-7-15-16		127	195	0.648434	0.04719	0.00800	0.06263	0.01050	0.00962	0.00023	62.0	10.0	62.0	1.0
LQL12-7-15-17		93	186	0.502180	0.04728	0.00780	0.06276	0.01030	0.00962	0.00024	62.0	10.0	62.0	2.0
LQL13-3-37-2	Granite porphyry	236	302	0.778681	0.04935	0.00672	0.06630	0.00733	0.01023	0.00030	65.2	7.0	65.6	1.9
LQL13-3-37-3		351	502	0.699681	0.04900	0.00569	0.06535	0.00639	0.01003	0.00025	64.3	6.1	64.3	1.6
LQL13-3-37-5		182	296	0.615249	0.05468	0.00729	0.07257	0.00696	0.01063	0.00034	71.1	6.6	68.2	2.2
LQL13-3-37-6		173	249	0.695012	0.05426	0.00820	0.06900	0.00879	0.01033	0.00040	67.8	8.4	66.3	2.6
LQL13-3-37-7		195	395	0.494821	0.04935	0.00722	0.06072	0.00750	0.00966	0.00024	59.9	7.2	62.0	1.5
LQL13-3-37-8		158	289	0.545933	0.05180	0.00629	0.06788	0.00608	0.01001	0.00032	66.7	5.8	64.2	2.0
LQL13-3-37-9		181	368	0.491539	0.05385	0.00681	0.07112	0.00706	0.01024	0.00028	69.8	6.7	65.7	1.8
LQL13-3-37-11		211	395	0.533911	0.05134	0.00561	0.07054	0.00651	0.01019	0.00026	69.2	6.2	65.3	1.7
LQL13-3-37-12		280	471	0.594531	0.04856	0.00490	0.06500	0.00526	0.00972	0.00022	63.9	5.0	62.4	1.4
LQL13-3-37-14		294	409	0.718215	0.05080	0.00677	0.06539	0.00749	0.00991	0.00026	64.3	7.1	63.6	1.7
LQL13-3-37-15		162	318	0.509264	0.05092	0.00657	0.06174	0.00621	0.00935	0.00027	60.8	5.9	60.0	1.7
LQL13-3-37-17		178	357	0.497456	0.05038	0.00808	0.06569	0.01041	0.01000	0.00028	64.6	9.9	64.1	1.8
LQL13-3-37-19		151	244	0.618356	0.05420	0.00692	0.07202	0.00754	0.00971	0.00025	70.6	7.1	62.3	1.6
LQL13-3-37-20		145	317	0.456904	0.05316	0.00837	0.06445	0.00924	0.00971	0.00028	63.4	8.8	62.3	1.8
LQL13-3-37-22		162	345	0.470072	0.04646	0.00707	0.06298	0.00622	0.01018	0.00028	62.0	5.9	65.3	1.8
LQL13-3-37-24		143	293	0.487149	0.04672	0.00690	0.06353	0.01081	0.00970	0.00028	62.5	10.3	62.2	1.8

Table 2

Re–Os analytical data of molybdenite samples from the Fe–Cu–(Mo) ore block in the Lietinggang-Leqingla deposit.

Samples	Weight (g)	Re (ng/g)		^{187}Re (ng/g)		^{187}Os (ng/g)		Model age (Ma)	
		Measured	1σ	Measured	1σ	Measured	1σ	Measured	1σ
LQL12-8-7	0.05062	31421.9	245.5	19749.3	154.3	19.5	0.2	59.2	0.8
LQL12-8-8	0.05007	42466.0	410.6	26687.0	255.9	26.2	0.3	59.6	0.7
LQL12-8-9	0.01455	15120.9	344.0	9503.8	216.2	9.5	0.1	60.0	1.6
LQL12-8-10	0.02000	48919.7	394.7	30747.0	248.1	30.5	0.3	59.4	0.8
LQL12-8-12	0.05023	74441.6	670.1	46788.0	421.2	46.6	0.5	59.7	0.9

Macquarie University). Concordia ages and diagrams were obtained using Isoplot/Ex (3.0) (Ludwig, 2003). The common lead was corrected using LA-ICP-MS Common Lead Correction (ver. 3.15), followed the method of Andersen (2002).

4.2. Re–Os dating

Five molybdenite samples were selected using an optical microscope and magnetically separated, with fresh, non-oxidized molybdenite (the purity more than 98%) separates with a 0.2–0.5 mm in diameter

Fig. 7. Re–Os isochron and model ages of molybdenite from the Lietinggang-Leqingla deposit.

handpicked using a binocular microscope. Re–Os isotope analyses were carried out in the Re–Os laboratory at the National Research Center of Geoanalysis, Chinese Academy of Geological Sciences in Beijing. A Carius tube (a thick-walled borosilicate glass ampoule) digestion was used. The weighed sample was loaded in a Carius tube through a thin neck long funnel. The mixed ^{190}Os and ^{185}Re spike solutions and 4 ml of 10 mol/L HCl and 4 ml of 16 mol/L HNO_3 were loaded while the bottom part of the tube was frozen at −80 to −50 °C in an ethanol-liquid nitrogen slush. The top was sealed using an oxygen-propane torch. The tube was then placed in a stainless-steel jacket and heated for 12 h at 230 °C. Upon cooling, the bottom part of the tube was kept frozen. Then the neck of the tube was broken, and the contents of the tube were poured into a distillation flask and the residue was washed out with 40 ml of water.

The Os was distilled twice. In the first distillation step, OsO_4 was distilled at 105–110 °C for 50 min and trapped in 10 ml of water. The residual Re-bearing solution was saved in a 150 ml beaker for Re separation. The water trap solution plus 40 ml of water were distilled a second time. The OsO_4 was distilled for 1 h and trapped in 10 ml of water that was used for ICP–MS (TJA PQEXCELL) determination of the Os isotope ratio. The Re-bearing solution was evaporated to dryness, and 1 ml of water was added twice while heating to near-dryness. Ten milliliters of 5 mol/L NaOH was added to the residue followed by Re extraction with 10 ml of acetone in a 120 ml Teflon separation funnel. The water phase was then discarded and the acetone phase was washed with 2 ml of 5 mol/L NaOH. The acetone phase was transferred to a 150 ml Teflon beaker that contained 2 ml of water. After evaporation to dryness, the Re was dissolved in 1 ml of water that was used for the ICP-MS determination of the Re isotope ratio. Cation-exchange resin was used to remove Na if the salinity of the Re-bearing solution was more than 1 mg/ml (Du et al., 2004). The decay constant of ^{187}Re of 1.666×10^{-11} per year used has an absolute uncertainty of ± 0.017 (1.0%, Smoliar et al., 1996).

4.3. Major and trace elements

Major element oxides, trace elements and rare earth elements (REEs) of the samples were analysed by X–ray fluorescence (XRF) and by inductively coupled plasma mass spectrometry (ICP–MS), respectively, at the National Research Centre for Geoanalysis, Chinese Academy of Geological Science (Beijing). The analytical uncertainty of XRF analyses for major elements was within 5 relative %, and the

uncertainty of the elements examined here was also less than 5 relative % for the ICP–MS analyses.

4.4. LA–MC–ICP–MS zircon Lu–HF isotope measurements

In situ Lu–Hf isotopic measurements were carried out on zircon grains with concordant ages within samples that were previously dated by LA–ICP–MS. *In situ* Lu–Hf analyses were performed by the LA–MC–ICPMS method using a Thermo Finnigan Neptune multi-collector-ICPMS and a Geolas CQ 193-nm laser ablation system housed at the Institute of Geology and Geophysics, Chinese Academy of Sciences, Beijing. The Lu–Hf isotopic analyses were performed on the same zircon grains that were previously analysed for U–Pb ages, with ablation pits of 63 μm in diameter and an ablation time of 26 s. Detailed descriptions of the analytical procedures can be found in Wu et al. (2006).

The results of ^{176}Hf/^{177}Hf for JMC475 Hf standard solution give an average ^{176}Hf/^{177}Hf ratio of 0.282158 ± 16 (n = 140, 2SD) normalized to ^{179}Hf/^{177}Hf = 0.7325 using an exponential law for mass bias correction (Wu et al., 2006). During laser ablation analyses, the isobaric interference of ^{176}Lu on ^{176}Hf is negligible due to the extremely low ^{176}Lu/^{177}Hf in zircon (normally < 0.002). However, the interference of ^{176}Yb on ^{176}Hf must be carefully corrected since the contribution of ^{176}Yb to ^{176}Hf could profoundly affect the accuracy of the measured ^{176}Hf/^{177}Hf ratio. In this project, the mean ^{173}Yb/^{171}Yb ratio of the individual spots was used to calculate the fractionation coefficient ($β_{Yb}$), and then to calculate the contribution of ^{176}Yb to ^{176}Hf. It is shown that this method can provide an accurate correction of the ^{176}Yb interference on ^{176}Hf (Woodhead et al., 2004; Wu et al., 2006; Kemp et al., 2009). During analysis, an isotopic ratio of ^{176}Yb/^{172}Yb = 0.5887 was applied (Wu et al., 2006). Standard zircon 91,500 was used for external correction. During analytical sessions, the obtained ^{176}Hf/^{177}Hf value of 91,500 was 0.282301 ± 8 (2σ), which was adjusted to 0.282305 (correction of 0.000004), a standard value recommended for 91,500 (Wu et al., 2006), although it is similar to the values obtained by the solution method, within error (Wiedenbeck et al., 1995; Woodhead et al., 2004; Davis et al., 2005). During data acquisition, analyses of TEMORA-2 as an unknown yielded a weighted ^{176}Hf/^{177}Hf ratio of 0.282673 ± 5 (2σ, n = 50), identical to the recommended value within error (Wu et al., 2006).

5. Results

5.1. U–Pb ages of the Jubuzhari complex intrusions

Zircon grains are separated from the samples of the granodiorite, granodiorite porphyry and granite porphyry with transparent, colorless to light brown, and mostly euhedral to subhedral (Fig. 6A, C, E). Zircons from these samples have consistent core-rim textures. We analyzed 16, 17 and 16 zircon grains from LQL13-4-5, LQL12-7-15 and LQL13-3-37 respectively (Table 1). In sample LQL13-4-5, the U contents vary from 215 to 890 ppm, the Th contents range from 975 to 1169 ppm, and the Th/U ratios are 0.44–1.31. The U contents in sample LQL12-7-15 are from 162 to 410 ppm, the Th contents vary from 72 to 300 ppm, and the Th/U ratios are 0.30–0.83. The U contents in sample LQL13-3-37 are from 244 to 502 ppm, the Th contents vary from 143 to 351 ppm, and the Th/U ratios are 0.46–0.78. The relatively high Th/U ratios and the well-developed oscillatory growth zoning indicate that these zircons are magmatic. Sixteen spot analyses carried out on zircons from sample LQL13-4-5 yielded similar ^{206}Pb/^{238}U ages ranging from 58.7 to 68.5 Ma, with a weighted age of 62.4 ± 1.2 Ma (MSWD = 1.7) (Fig. 6B), which is interpreted as the crystallization age of the granodiorite. Seventeen spot analyses of sample LQL12-7-15 yield similar ^{206}Pb/^{238}U ages ranging from 61.0 to 64.0 Ma, with a weighted age of 62.6 ± 0.6 Ma (MSWD = 0.8) (Fig. 6D), interpreted as the crystallization age of the granodiorite porphyry. Sixteen zircon analyses of

Table 3

Major and trace elements analysis of the granodiorite, granodiorite porphyry, and granite porphyry in the Lietinggang-Leqingla deposit.

Samples	LQL13-4-5-1	LQL13-4-5-5	LQL12-6-1	LQL12-6-2	LQL12-6-3	LQL12-6-5	LQL12-6-6	LTG13-3-37-4	LTG13-3-37-5	LTG13-3-37-6
Rock type	Granodiorite		Granodiorite porphyry					Granite porphyry		
SiO_2 (%)	61.96	69.11	73.34	73.69	73.98	72.33	73.44	75.76	74.82	75.08
Al_2O_3	15.28	15.07	13.49	13.32	13.07	13.75	13.39	12.84	13.08	12.88
TFeO	5.24	3.06	2.31	2.11	2.15	2.60	2.24	1.44	1.44	1.63
CaO	5.00	2.78	1.28	1.15	1.16	1.03	1.19	0.55	0.59	0.73
MgO	1.73	0.77	0.36	0.33	0.32	0.36	0.32	0.13	0.15	0.25
K_2O	2.14	3.21	3.84	3.92	3.98	4.19	3.88	4.46	4.59	4.20
Na_2O	4.49	4.25	4.12	4.13	3.91	3.99	4.11	4.09	4.14	4.12
MnO	0.18	0.04	0.04	0.03	0.04	0.05	0.03	0.02	0.02	0.04
TiO_2	0.65	0.38	0.22	0.21	0.22	0.22	0.22	0.12	0.15	0.16
P_2O_5	0.22	0.12	0.06	0.06	0.06	0.06	0.05	0.02	0.03	0.04
LOI	2.36	0.69	0.59	0.66	0.72	0.99	0.72	0.29	0.69	0.54
Total	99.84	99.83	99.91	99.84	99.84	99.86	99.85	99.88	99.86	99.86
DI	67.13	78.40	89.30	90.34	90.21	89.57	89.88	94.49	94.28	93.02
A/CNK	0.81	0.97	1.02	1.01	1.02	1.06	1.02	1.02	1.02	1.02
A/NK	1.57	1.44	1.23	1.21	1.22	1.24	1.22	1.11	1.11	1.14
Rb (ppm)	58.7	71.3	134	132	130	146	124	112	115	119
Sr	493	243	145	152	124	163	148	72.1	64.7	98.9
Y	46.1	15.5	34.8	33.3	31.7	30.4	29.1	25.8	31.9	34.9
Zr	64.1	28.6	131	174	148	104	101	39.7	100	104
Nb	15.8	6.44	10.5	10.0	9.56	9.35	9.45	10.4	11.7	11.3
Cs	1.92	1.85	2.67	2.23	2.73	2.97	1.99	1.58	2.13	1.83
Ba	431	613	656	682	664	668	678	635	706	657
La	17.9	40.6	42.8	34.3	33.9	36.5	35.4	36.6	37.1	37.2
Ce	44.3	79.5	87.0	73.8	70.1	75.2	72.7	79.4	79.6	80.7
Pr	6.37	8.39	10.03	8.51	8.29	8.70	8.51	9.34	9.28	9.36
Nd	28.2	26.8	37.2	32.1	31.9	33.3	32.5	34.3	34.3	33.4
Sm	6.91	6.03	7.36	6.74	6.44	6.51	6.17	7.05	7.04	6.57
Eu	1.08	1.14	1.00	0.99	0.93	1.06	0.95	0.76	0.78	0.78
Gd	7.49	4.21	6.12	5.60	5.34	5.30	5.06	6.14	6.46	6.64
Tb	1.32	0.56	1.01	0.97	0.92	0.9	0.86	0.92	1.03	1.06
Dy	8.39	3.02	6.05	5.77	5.54	5.32	5.19	5.30	6.07	6.41
Ho	1.82	0.61	1.22	1.16	1.14	1.09	1.05	1.08	1.27	1.36
Er	5.35	1.70	3.67	3.52	3.46	3.39	3.24	3.14	3.71	4.01
Tm	0.89	0.26	0.63	0.60	0.60	0.59	0.57	0.51	0.61	0.67
Yb	6.06	1.79	4.26	3.96	4.02	3.87	3.76	3.47	4.13	4.49
Lu	0.92	0.27	0.65	0.62	0.62	0.6	0.58	0.53	0.64	0.70
Hf	2.16	1.06	4.24	5.17	4.62	3.46	3.40	1.62	3.85	3.91
Ta	0.78	0.48	0.91	0.82	0.81	0.83	0.83	0.96	1.04	1.09
Pb	25.1	11.1	45.8	36.8	40.7	48.6	45.6	29.2	33.2	37.3
Th	6.26	7.94	14.4	13.8	14.2	13.6	14.1	15.7	14.8	16.1
U	1.94	0.81	3.65	3.44	3.38	3.07	3.41	1.92	2.47	3.76
V	66.0	29.7	18.3	21.9	9.65	11.5	9.39	1.26	1.98	3.22
Cr	1.28	1.36	26.19	36.24	5.09	5.51	3.54	0.02	0.06	0.84
Co	6.01	3.61	1.13	0.98	0.97	1.00	1.08	0.62	0.42	0.58
Ni	1.55	1.14	0.44	0.38	0.35	0.31	0.32	0.15	0.30	0.19
δEu	0.46	0.66	0.46	0.49	0.48	0.55	0.52	0.35	0.35	0.36

Notes: A/CNK = $Al_2O_3/(CaO + Na_2O + K_2O)$ (molar ratio), A/NK = $Al_2O_3/(Na_2O + K_2O)$ (molar ratio), DI = Quartz + Orthoclase + Albite + Nepheline + Leucite + K-feldspar, from CIPW calculating values; LOI, loss on ignition. $\delta Eu = w(Eu)/w(Eu^*) = w(Eu)_N/[(1/2)/(w(Sm)_N/(w(Gd)_N)]$, where $w(Eu)_N$, $w(Sm)_N$, $w(Gd)_N$ are chondrite-normalized.

sample LQL13-3-37, yielded similar $^{206}Pb/^{238}U$ ages ranging from 60.0 to 68.2 Ma, and formed a weighted age of 63.7 ± 1.0 Ma (MSWD = 1.2) (Fig. 6F), which is interpreted as the crystallization age of the granite porphyry.

5.2. Re–Os dating results of the molybdenite

The Re and Os abundances and isotopic data for molybdenite samples are presented in Table 2. Total Re and ^{187}Os concentrations vary from 15.12 to 74.44 ppm and from 0.01 to 0.05 ppm, respectively. The Re–Os model ages of the five molybdenites range from 59.2 ± 0.9 to 60.0 ± 1.6 Ma with a weighted model age of 59.6 ± 1.0 Ma (MSWD = 0.13) (Fig. 7). The isochron age for all fore samples calculated with ISOPLOT software (Ludwig, 2003) is 59.0 ± 1.7 Ma with a MSWD of 1.6 (Fig. 7), which is interpreted as the age of molybdenite crystallization during the formation of the Lietinggang-Leqingla deposit.

5.3. Major and trace element compositions of whole rocks

Major and trace elements of the Jubuzhari complex are given in Table 3. Samples from the complex can be classified into two groups (moderately fractionated and strongly fractionated) on the basis of geochemical compositions. Rocks from the granodiorite have relatively lower SiO_2 (62.0–69.1 wt%), and total alkali content (K_2O + Na_2O = 6.63–7.46 wt%), plotting in the granodiorite field (Fig. 8A). K_2O content of the granodiorites ranges from 2.14 to 3.21 wt%, belonging to High-K calc-alkaline affinity (Fig. 8B). The granodiorites have Al_2O_3 content of 15.1–15.3 wt%, and A/CNK [molar $Al_2O_3/$ $(CaO + Na_2O + K_2O)$] ranging from 0.81 to 0.97, indicating that they are metaluminous (Fig. 8C). The granodiorites are moderately fractionated in composition as indicated by a differentiation index (DI) (DI = Quartz + Orthoclase + Albite + Nepheline + Leucite + K-feldspar, from CIPW calculating values) of 67–78 (Fig. 8D). The granodiorite porphyries include five granite samples (Fig. 8A), which have
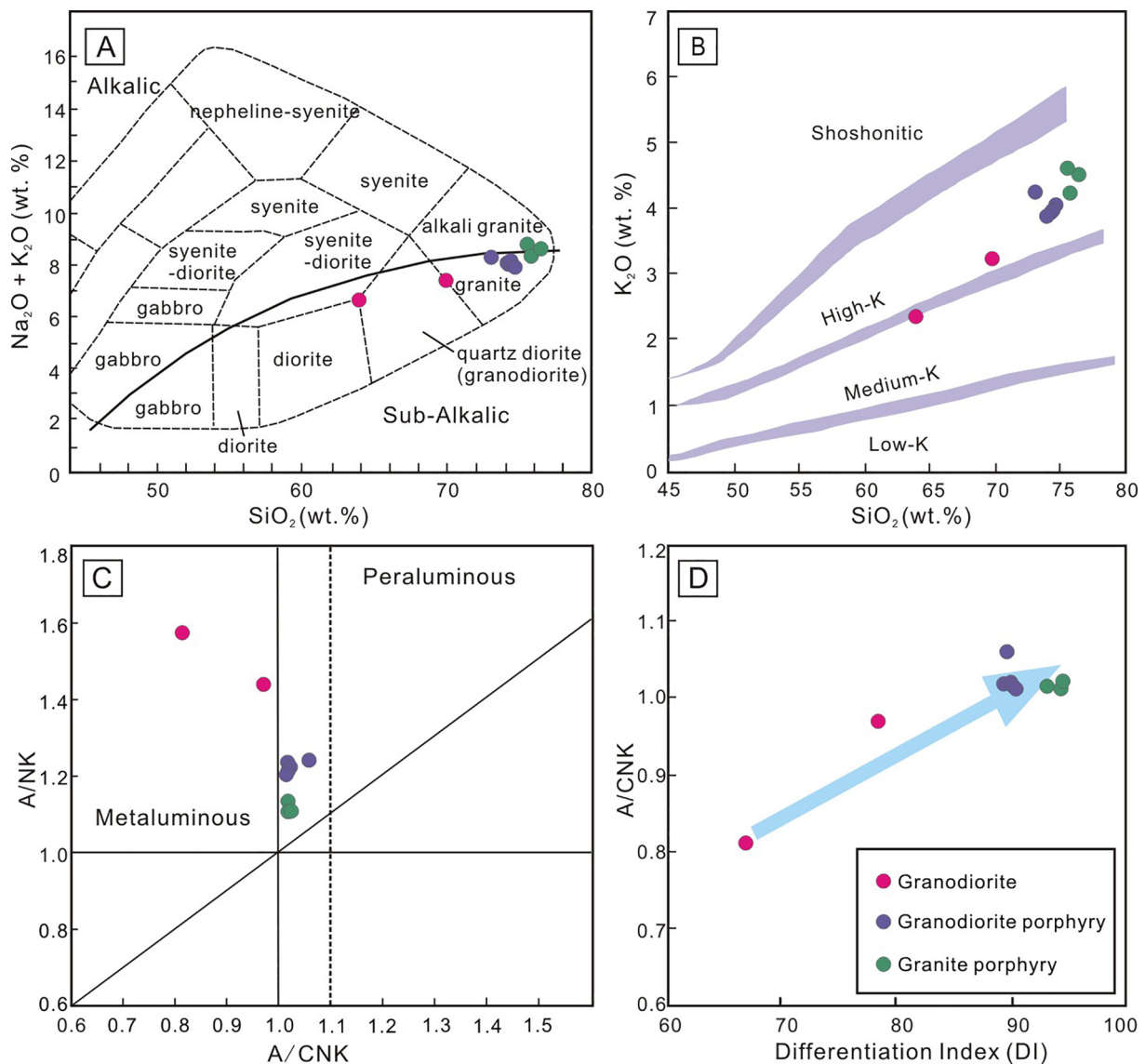
Fig. 8. A) TAS diagram, according to Wilson (2001); B) K_2O versus SiO_2 diagram (Rickwood, 1989); C) A/CNK versus A/NK diagram; D) A/CNK versus differentiation index (DI) diagram for the ore-forming rocks from Lietinggang-Leqingla deposit. A/CNK = Al_2O_3/(CaO + Na_2O + K_2O) (molar ratio), A/NK = Al_2O_3/(Na_2O + K_2O) (molar ratio), DI = Quartz + Orthoclase + Albite + Nepheline + Leucite + K-feldspar, from CIPW calculating values.

High-K calc-alkaline affinity with K_2O of 3.84–4.19 wt% (Fig. 8B). These samples have relatively higher SiO_2 of 72.3–74.0 wt% and A/CNK ratios (1.01–1.06) than that of the granodiorites. They located between metaluminous and peraluminous (Fig. 8C) with strongly fractionated in composition as indicated by a differentiation index (DI) of 89–90 (Fig. 8D). The granite porphyries consist of three high-K calc-alkaline granite samples (Fig. 8A, B). The Al_2O_3 content ranges from 12.8 wt% to 13.1 wt%, with A/CNK ranging from 1.01 to 1.02, belonging to metaluminous to weakly peraluminous (Fig. 8C). It is strongly fractionated granite in composition, as indicated by its high SiO_2 (74.8–75.8 wt%) and DI (93–94) (Fig. 8D). CaO, Al_2O_3, MgO, Fe_2O_3, P_2O_5, and TiO_2 contents of the three types of intrusions in the Jubuzhari complex show negative correlations with SiO_2 (Fig. 9).

Rocks from the three types of intrusions all exhibit moderately fractionated REE patterns, characterized by lower contents of heavy REE (HREE) relative to light REE (LREE) with moderately negative Eu anomalies (δEu = 0.35–0.66) [δEu = w(Eu)/w(Eu*) = w(Eu)$_N$/[(1/2)/(w(Sm)$_N$/(w(Gd)$_N$)]], where w(Eu)$_N$, w(Sm)$_N$, w(Gd)$_N$ are chondrite-normalized] (Fig. 10A; Table 3). Compared to rocks from the granodiorite and granodiorite porphyry (δEu = 0.46–0.66 and 0.46–0.55),

the granite porphyries have the most negative Eu anomalies (δEu = 0.35–0.36). In trace elements, rocks from the granodiorite, granodiorite porphyry, and granite porphyry all exhibit similar patterns in the primitive mantle-normalized spidergrams (Fig. 10B). Meanwhile, they are also enriched in large-ion lithophile elements (e.g., Rb, Ba, Pb, K and Th) and depleted in high-field-strength elements (e.g., Ta, Ti and Nb) (Fig. 10B).

5.4. In situ zircon Hf isotope analyses

Lu-Hf isotopic analyses of zircons from rocks of the granodiorite, granodiorite porphyry and granite porphyry were conducted on the same grains with U–Pb ages. The results are listed in Table 4 and Fig. 11.

Thirteen spot analyses were obtained for LQL13-4-5 from granodiorite, yielding $^{176}Hf/^{177}Hf$ isotopic ratios from 0.282807 to 0.282973, and $ε_{Hf(t)}$ values from +2.5 to +8.4, with TC DM model ages of 599–973 Ma. Thirteen spot analyses were obtained for LQL12-7-15 from the granodiorite porphyry, yielding $^{176}Hf/^{177}Hf$ isotopic ratios from 0.282557 to 0.282927, and $ε_{Hf(t)}$ values from −6.3 to +6.8, with
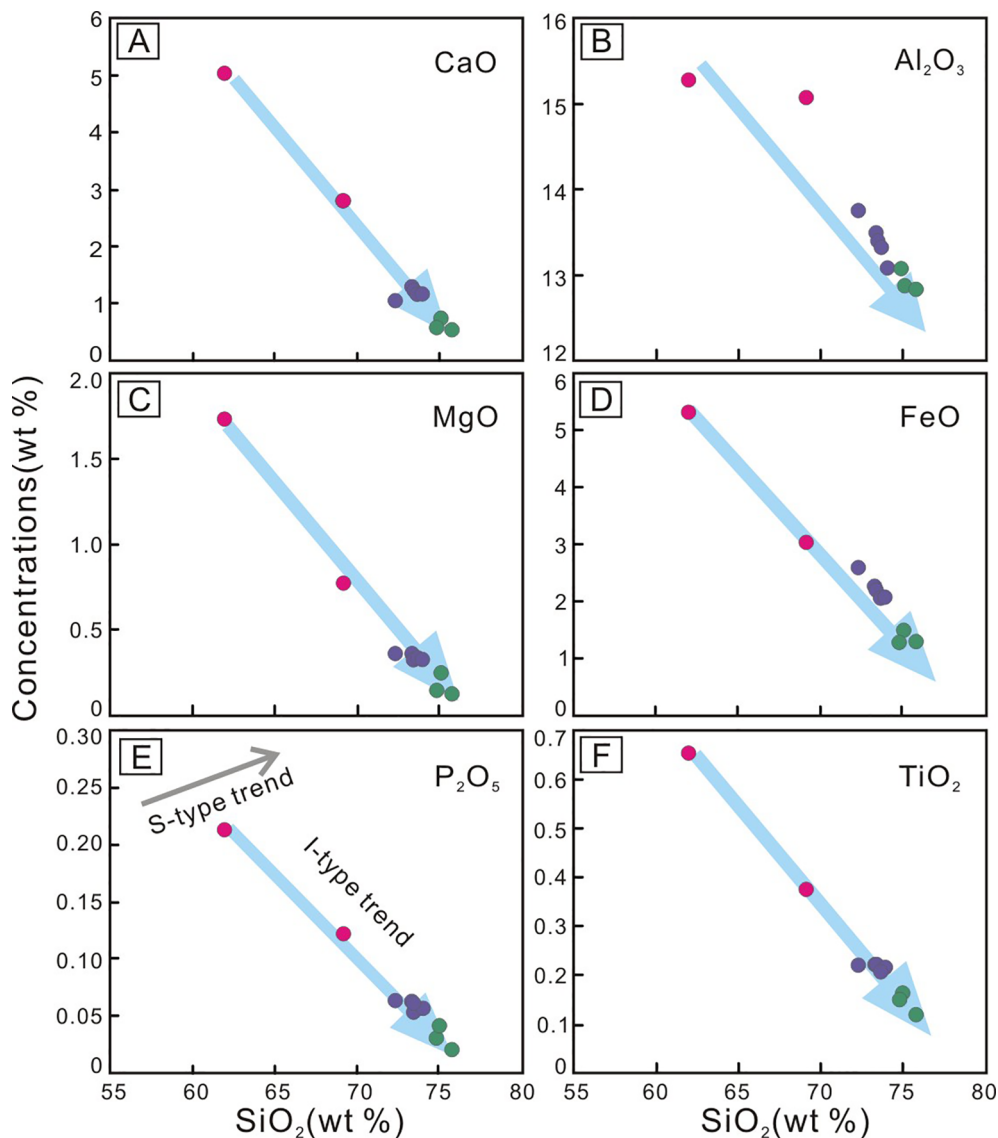
Fig. 9. Harker variation diagrams showing the major element variations in the ore-forming rocks from the Lietinggang-Leqingla deposit.
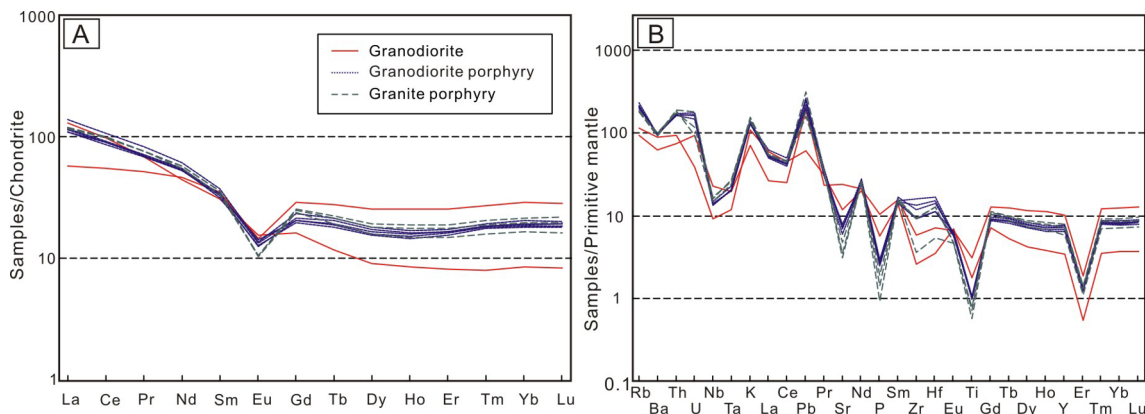

Fig. 10. A) Chondrite-normalized REE patterns and B) Primitive mantle-normalized patterns for the ore-forming rocks from the Lietinggang-Leqingla deposit. Primitive mantle and chondrite normalization factors are from Sun and McDonough (1989).

TC DM model ages of 696–1522 Ma. Thirteen spot analyses were obtained for LQL13-3-37 from granite porphyry, yielding $^{176}Hf/^{177}Hf$ isotopic ratios from 0.282788 to 0.282932, and $\varepsilon_{Hf(t)}$ values from +1.8 to +6.9, with TC DM model ages of 696–1018 Ma.

5.5. Zircon trace elements

The zircon trace elements are listed in Table 5, and the chondrite-normalized REE patterns are shown in Fig. 12A–C. Most of the zircon

Table 4

Hf isotopic data of zircons from the granodiorite, granodiorite porphyry, and granite porphyry in the Lietinggang-Leqingla deposit.

Samples	Rock type	Age/Ma	$^{176}Lu/^{177}Hf$	2σ	$^{176}Hf/^{177}Hf$	2σ	$\varepsilon_{Hf}(t)$	T_{DM}/Ma	$T_{DM}{}^{C}$/Ma	$f_{Lu/Hf}$
LQL13-4-5-2	Granodiorite	63.1	0.001665	0.000016	0.282826	0.000030	3.22	615	929	−0.95
LQL13-4-5-3		63.1	0.001885	0.000012	0.282905	0.000028	6.01	504	750	−0.94
LQL13-4-5-4		60.1	0.002162	0.000011	0.282885	0.000030	5.18	537	800	−0.93
LQL13-4-5-5		65.1	0.001668	0.000012	0.282812	0.000024	2.77	635	960	−0.95
LQL13-4-5-6		62.2	0.002020	0.000012	0.282868	0.000022	4.69	559	834	−0.94
LQL13-4-5-7		59.8	0.001916	0.000054	0.282930	0.000026	6.82	468	696	−0.94
LQL13-4-5-11		58.7	0.001966	0.000033	0.282872	0.000026	5.05	553	820	−0.94
LQL13-4-5-14		65.1	0.002019	0.000006	0.282807	0.000028	2.52	648	973	−0.94
LQL13-4-5-15		63.1	0.001856	0.000015	0.282844	0.000022	3.87	591	888	−0.94
LQL13-4-5-17		62.9	0.002981	0.000011	0.282933	0.000029	6.94	477	690	−0.91
LQL13-4-5-18		63.6	0.003185	0.000016	0.282973	0.000028	8.38	419	599	−0.90
LQL13-4-5-21		60.7	0.002922	0.000052	0.282851	0.000027	4.02	598	876	−0.91
LQL13-4-5-23		62.7	0.003115	0.000041	0.282964	0.000028	8.04	432	620	−0.91
LQL12-7-15-1	Granodiorite porphyry	62.0	0.001423	0.00002	0.282831	0.00002	3.46	603	909	−0.96
LQL12-7-15-2		62.0	0.001407	0.000015	0.282785	0.000015	1.77	669	1014	−0.96
LQL12-7-15-4		64.0	0.001435	0.00002	0.282854	0.00002	4.18	571	860	−0.96
LQL12-7-15-5		61.0	0.002288	0.000021	0.282927	0.000021	6.79	477	696	−0.93
LQL12-7-15-6		63.0	0.00134	0.000018	0.282772	0.000018	1.27	687	1045	−0.96
LQL12-7-15-7		62.0	0.001048	0.000016	0.282798	0.000016	2.25	645	985	−0.97
LQL12-7-15-8		63.0	0.003203	0.00002	0.282884	0.00002	5.18	554	797	−0.90
LQL12-7-15-10		62.0	0.000967	0.000019	0.282862	0.000019	4.51	553	841	−0.97
LQL12-7-15-11		64.0	0.001254	0.00002	0.282557	0.00002	−6.25	990	1522	−0.96
LQL12-7-15-12		62.0	0.001559	0.000018	0.282848	0.000018	4.00	581	873	−0.95
LQL12-7-15-13		61.0	0.001646	0.00002	0.282781	0.00002	1.67	679	1022	−0.95
LQL12-7-15-15		61.0	0.000946	0.00002	0.282797	0.00002	2.19	645	987	−0.97
LQL12-7-15-16		62.0	0.001142	0.000017	0.282797	0.000017	2.19	647	987	−0.97
LQL13-3-37-2	Granite porphyry	65.6	0.003350	0.000050	0.282912	0.000028	6.25	514	737	−0.90
LQL13-3-37-5		68.2	0.002815	0.000060	0.282799	0.000026	2.32	675	991	−0.92
LQL13-3-37-7		62.0	0.001944	0.000015	0.282928	0.000028	6.81	471	699	−0.94
LQL13-3-37-8		64.2	0.004395	0.000019	0.282932	0.000037	6.87	499	696	−0.87
LQL13-3-37-9		65.7	0.001766	0.000009	0.282882	0.000024	5.24	536	802	−0.95
LQL13-3-37-11		65.3	0.001376	0.000009	0.282829	0.000029	3.39	606	920	−0.96
LQL13-3-37-12		62.4	0.003076	0.000086	0.282844	0.000045	3.79	612	892	−0.91
LQL13-3-37-14		63.6	0.001669	0.000011	0.282895	0.000028	5.66	516	773	−0.95
LQL13-3-37-15		60.0	0.002504	0.000018	0.282788	0.000030	1.79	685	1018	−0.92
LQL13-3-37-17		64.1	0.001419	0.000022	0.282794	0.000029	2.14	656	999	−0.96
LQL13-3-37-20		62.3	0.001743	0.000030	0.282806	0.000029	2.51	644	974	−0.95
LQL13-3-37-22		65.3	0.001811	0.000006	0.282851	0.000029	4.15	581	872	−0.95
LQL13-3-37-24		62.2	0.002325	0.000005	0.282854	0.000030	4.18	584	867	−0.93

$T_{DM} = (1/\lambda) \times \ln(1 + ((^{176}Hf/^{177}Hf)_s - (^{176}Hf/^{177}Hf)_{DM})/((^{176}Lu/^{177}Hf)_s - (^{176}Lu/^{177}Hf)_{DM}));$ $T_{DM}{}^{C} = T_{DM} - ((T_{DM} - t) \times ((f_{cc} - f_s)/(f_{cc} - f_{DM})).$ $\lambda = 1.867 \times 10^{-11}$ year^{-1}; $(^{176}Lu/^{177}Hf)_{DM} = 0.0384.$ $(^{176}Hf/^{177}Hf)_{DM} = 0.28325$ (Griffin et al., 2000); $f_{cc} = -0.5482$ (Griffin et al., 2000); $f_{DM} = 0.157.$

grains are depleted in LREE and enriched in HREE on chondrite normalized patterns and are characterized by positive Ce anomalies with variable negative Eu anomalies. Zircon is a widespread accessory mineral in intermediate to felsic igneous rocks and is resistant to hydrothermal alteration and physical and chemical weathering (Hoskin and Schaltegger, 2003). Ce and Eu in zircons commonly are sensitive to magmatic oxidation state due to multiple ionic states. Here, we calculate zircon Ce^{4+}/Ce^{3+} ratios and ΔFMQ values by the methods of Ballard et al. (2002) and Qiu et al. (2013). The compositions of the whole-rock samples are assumed to represent those of the parental melt. The partition coefficients for Ce^{4+} and Ce^{3+} can be estimated on the basis of crystal chemical constraints on trace element partitioning of the REEs (Nd to Lu), Hf, U and Th between zircon and whole rock (Blundy and Wood, 1994). The detailed description is described by Ballard et al. (2002) and Qiu et al. (2013). The Eu anomalies (Eu_N/Eu_N*) are calculated by a conventional method based on normalized values of Sm and Gd concentrations ($Eu_N* = (Sm_N * Gd_N) * 1/2$). Temperatures of magma are estimated using the Ti-in-zircon thermometer (Watson et al., 2006; Ferry and Watson, 2007). The calculated temperatures of granodiorite (LQL13-4-5) are from 648 °C to 753 °C, with an average of 690 °C (Fig. 13D). The granodiorite porphyry (LQL12-7-15) yields temperature range of 658–751 °C with an average of 693 °C (Fig. 13D). The calculated temperatures of granite porphyry (LQL13-3-37-4) demonstrate a wide range from 611 °C to 792 °C with an average of 685 °C (Fig. 13D).

The oxidation state of the Lietinggang-Leqingla magmas has been investigated using geochemical parameter. Zircons grains from the granodiorite display relatively low Ce^{4+}/Ce^{3+} ratios (average = 72.08; Fig. 12F), and Eu_N/Eu_N* ratios are below 0.40 (average = 0.20, Fig. 13F), and the ΔFMQ values range from −3.43 to 4.25 with an average of 0.15 (Fig. 13D, E). For the granodiorite porphyry, the zircon grains have lower Ce^{4+}/Ce^{3+} ratios (average = 62.16) (Fig. 13F), and ΔFMQ values (average = −0.07) (Fig. 13D, E), with slightly higher Eu_N/Eu_N* values from 0.15 to 0.37 (average = 0.22) (Fig. 13F). The zircon grains of granite porphyry have the lowest Ce^{4+}/Ce^{3+} ratios (average = 55.51) (Fig. 13F) and ΔFMQ values (varying from −7.47 to 3.31 with an average of −1.09) (Fig. 13D, E), but the Eu_N/Eu_N* values are becoming higher, ranging from 0.12 to 0.42 with an average of 0.25 (Fig. 13F). In general, the oxidation state of the magma decreased gradually from the granodiorite to granite porphyry.

6. Discussion

6.1. Ages of magmatism and mineralization

LA–ICP–MS U–Pb zircon dating of the Jubuzhari complex indicates that the crystallization ages of the granodiorite and granodiorite porphyry are 62.4 ± 1.2 Ma (Fig. 6B), and 62.6 ± 0.6 Ma (Fig. 6D), respectively, while the granite porphyry is 63.7 ± 1.0 Ma (Fig. 6F). Re–Os analyses obtained for molybdenite yield identical model ages
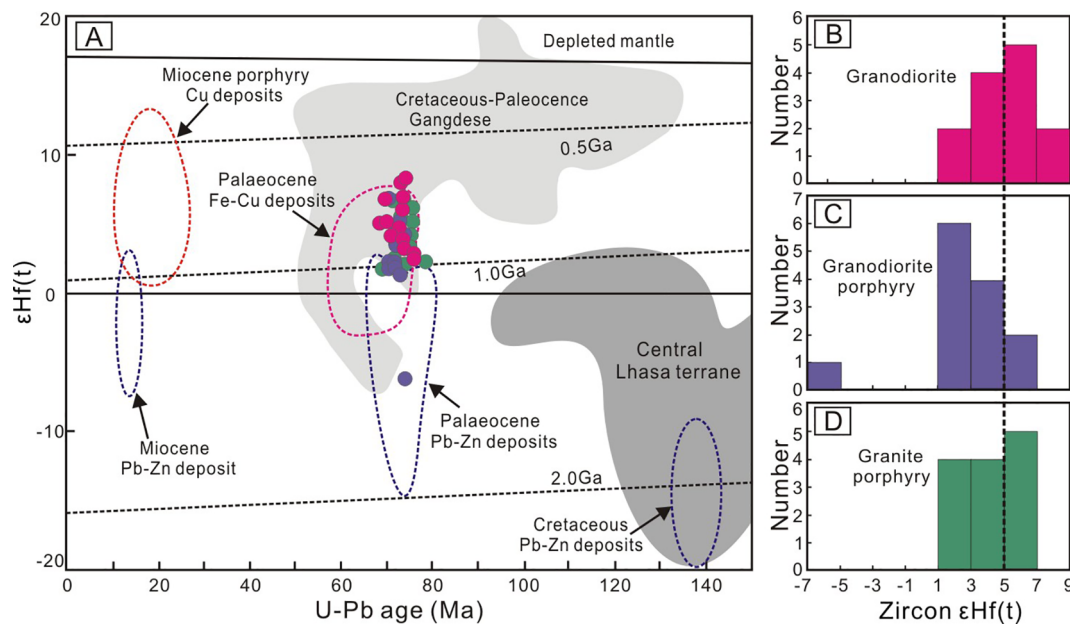
Fig. 11. A) $\varepsilon_{Hf(t)}$ versus U–Pb ages and B) Histogram of $\varepsilon_{Hf(t)}$ from the ore-forming rocks in the Lietinggang-Leqingla deposit. Data of the Cretaceous Pb–Zn deposits from Gao et al. (2011); Data of the Paleocene Pb–Zn deposits from Zheng et al. (2015); Data of the Paleocene Fe–Cu deposits from Fu et al. (2013) and Zheng et al. (2015); Data of the Miocene Pb–Zn deposit from Fu et al. (2017); Data of the Miocene porphyry Cu deposits from Chung et al. (2009), Hou et al. (2013), and Li et al. (2011).

(weighted mean age = 59.6 ± 1.0 Ma, MSWD = 0.13) and isochron age (59.0 ± 1.7 Ma, MSWD = 1.6) (Fig. 7), indicates that the Lietinggang-Leqingla Fe–Cu–(Mo)–Pb–Zn mineralization took place at ~59 Ma. Together with the geological characteristics (the mineralization occurred in the contact zone between the Jubuzhari complex intrusions and strata of the Mengla Formation), the almost identical ages constraint between the intrusions and mineralization indicate that the Jubuzhari complex is the ore-forming rocks of the Lietinggang-Leqingla skarn Fe–Cu–(Mo)–Pb–Zn polymetallic deposit. Therefore, magmatism and the Fe–Cu–(Mo)–Pb–Zn mineralization in the Lietinggang-Leqingla deposit are developed during or shortly before the main stage of the Indian–Asian continental collision (Mo et al., 2005; Hou et al., 2006a; Hou and Cook, 2009; Zhu et al., 2015), which is consistent with the main mineralization period of regional Fe–Cu, Pb–Zn and Mo mineralization throughout the Lhasa terrane (Fig. 1C; Fu et al., 2017; Zheng et al., 2015).

6.2. Petrogenesis of the ore-forming rocks

6.2.1. Source of the ore-forming rocks

A large abundance of hornblende, relatively low-medium Al_2O_3 contents, and metaluminous in nature (Fig. 8C) suggest that the granodiorites are typical I-type granites ($Na_2O > 3.2$ wt% and A/CNK < 1.1) (Chappell and White, 1974). The relationship between P_2O_5 and SiO_2 is generally considered as a proxy to determine the petrogenetic type of granites (Chappell, 1999; Li et al., 2007; Wu et al., 2003a), because of that P_2O_5 abundances will reduce in fractionated I-type granites as apatite reaches saturation in metaluminous or mildly peraluminous magmas (Chappell, 1999; Li et al., 2007; Montel et al., 1988). Thus, negative trend of P_2O_5 vs. SiO_2 of rocks from the granodiorite, granodiorite porphyry and granite porphyry (Fig. 9E), together with the absence of minerals that generally occur in S-type granites (e.g., muscovite), suggests an affinity to I-type granite in the Jubuzhari complex (Chappell, 1999; Li et al., 2007; Wu et al., 2003a). This is also consistent with the trace elements results for these samples.

Chappell and White (1992) suggested that La and Ce contents remain constant in I-type granites, whereas these elements decrease in S-type granites, as the Rb contents increasing. Moreover, Y increases

substantially with crystal fractionation in I-type granites, but remains relatively constant in S-type granites. Rocks from the Jubuzhari complex show I-type granite trends in La, Ce, and Y when plotted against Rb (Fig. 13). High A/CNK ratios may suggest that the granodiorite porphyries and granite porphyries, belonging to metaluminous to weakly peraluminous, have an affinity to S-type granite (Chappell and White, 1974). However, we consider that they are not S-type granite because the high ratios of A/CNK probably resulted from fractionation of feldspar by a significant decrease in CaO (Fig. 9A).

Three models have been reconstructed to analyze the petrogenesis of the moderately fractionated calc-alkaline I-type granites: (1) advanced assimilation and fractional crystallization of mantle derived basaltic parental magmas (Bacon and Druitt, 1988; Beard and Lofgren, 1991; Grove et al., 1997; Sisson et al., 2005), (2) partial melting of mafic to intermediate meta-igneous crustal rocks with or without addition of mantle-derived mafic magmas (Chappell and Stephens, 1988; Chappell and White, 2001; Li et al., 2007; Petford and Atherton, 1996), and (3) reworking of supra-crustal materials with varying contributions from mantle derived magmas (Collins and Richards, 2008; Kemp et al., 2007). The rocks produced by fractional crystallization from basaltic parental magmas generally have a wide range in composition and inflexions of elements on variation diagrams, including the occurrence of abundant cumulate rocks (e.g. Keller et al., 2015), such as the I-type Boggy Plain Supersuite granites from the Lachlan Fold Belt (Chappell, 1999) and the Cordillera arc in the North American margin (e.g. Lee et al., 2007). However, the Jubuzhari intrusions are exclusively felsic without mafic to intermediate varieties. Furthermore, in a regional context, the 63 ± 3 Ma magmatism in the central Lhasa subterrane is also dominated by felsic compositions (e.g. Ji et al., 2009, 2012a; Zhu et al., 2011; Zheng et al., 2015), with rare occurrence of mafic rocks and cumulates, precluding that the Jubuzhari complex rocks were generated by fractional crystallization of basaltic parental magmas. It is also unlikely that the reworking of supracrustal materials with varying contributions from mantle-derived magmas (Collins and Richards, 2008; Kemp et al., 2007) can account for the petrogenesis of moderately fractionated granodiorites because this mechanism will produce zircons with a wide range of $\varepsilon_{Hf(t)}$ values (up to 10-ε units) within a single rock sample (e.g., Kemp et al., 2007), which is not the case for the

Table 5
Zircon trace element analysis result of the granodiorite, granodiorite porphyry and granite porphyry in the Lietinggang-Leqingla deposit.

Sample spot	La	Ce	Pr	Nd	Sm	Eu	Gd	Tb	Dy	Ho	Er	Tm	Yb	Lu	Ti	Hf	U	Th	ΔFMQ^*	Ce^{4+}/Ce^{3+}	Eu_N/Eu_N^*	δCe	$lg(fO_2)$	T (°C)
Granodiorite																								
LQL13-4-5-1	0.21	19.37	0.18	1.74	4.02	0.52	28.88	10.37	135.95	54.06	252.15	52.56	484.61	97.09	3.79	10532.94	500.91	288.99	0.99	98.52	0.15	67.22	−16.85	662
LQL13-4-5-3	8.80	36.94	2.78	14.46	5.75	0.38	19.27	6.71	88.01	35.29	171.96	37.08	354.88	72.81	4.46	11176.58	321.38	153.78	−3.13	22.06	0.11	20.28	−20.63	675
LQL13-4-5-6	0.00	16.31	0.10	1.22	3.21	0.53	22.30	8.61	112.53	44.07	211.23	44.61	412.99	84.19	3.49	9358.08	391.06	255.40	1.56	123.24	0.19	82.42	−16.45	656
LQL13-4-5-8	0.17	16.36	0.17	1.85	4.59	1.29	32.48	12.54	161.20	68.23	321.90	70.16	671.68	139.70	4.12	8783.47	325.82	186.51	0.78	90.34	0.32	60.39	−16.89	669
LQL13-4-5-9	0.16	22.63	0.21	2.39	6.56	1.39	37.07	13.32	169.08	72.06	357.87	83.81	872.78	197.98	3.11	8187.19	666.74	579.81	0.48	97.48	0.27	66.48	−17.78	648
LQL13-4-5-10	0.06	35.56	0.30	4.44	10.70	2.44	60.07	21.29	259.16	105.52	506.09	114.60	1143.30	246.17	5.23	7696.01	889.62	1169.47	0.59	70.13	0.29	49.43	−16.58	687
LQL13-4-5-12	17.44	59.37	5.78	24.74	8.91	1.31	30.50	11.41	150.05	60.99	300.70	68.69	680.10	148.05	3.36	11328.49	623.83	281.29	−3.43	24.62	0.24	22.35	−21.53	653
LQL13-4-5-13	2.38	15.69	0.90	5.81	3.82	0.45	17.20	6.34	80.90	34.02	159.38	34.78	341.27	70.68	8.98	10597.73	214.88	97.37	−1.25	25.88	0.17	21.55	−17.29	732
LQL13-4-5-14	0.03	15.47	0.08	0.98	3.50	0.41	23.11	8.88	113.33	46.66	227.42	47.82	452.44	93.64	4.00	10037.33	369.15	163.43	2.36	143.77	0.14	93.61	−15.37	666
LQL13-4-5-15	7.09	33.84	2.41	12.17	5.82	0.48	23.35	8.77	112.56	45.74	207.54	42.92	401.76	81.48	8.33	10351.17	394.23	203.50	−1.54	23.78	0.13	20.90	−17.73	725
LQL13-4-5-16	0.58	24.36	0.31	3.59	7.16	1.76	47.55	18.81	241.17	101.35	482.17	103.77	970.47	199.81	8.86	9014.54	513.28	327.04	1.68	68.72	0.29	47.37	−14.39	730
LQL13-4-5-21	0.22	23.18	0.17	1.67	5.09	0.33	30.74	12.28	155.18	63.81	296.33	61.66	570.27	116.29	11.42	10649.23	811.42	461.64	4.25	119.40	0.08	79.95	−11.29	753
LQL13-4-5-22	4.91	32.25	1.61	10.05	5.92	0.68	33.56	11.55	151.34	59.59	273.13	57.89	526.09	108.04	7.13	10332.98	482.34	309.62	−1.37	29.15	0.15	24.10	−17.90	712
Granodiorite porphyry																								
LQL12-7-15-01	0.92	10.30	0.29	2.79	3.84	0.69	19.80	7.33	95.25	37.22	164.55	40.33	462.09	86.91	6.05	9239.84	202.70	106.31	−1.34	34.17	0.24	26.93	−18.21	699
LQL12-7-15-02	0.60	14.65	0.33	2.46	3.17	0.48	16.21	6.31	80.60	31.89	141.64	34.74	398.61	74.60	4.87	9129.54	164.99	75.99	0.10	58.02	0.21	45.25	−17.22	681
LQL12-7-15-03	0.10	7.93	0.08	0.89	2.71	0.33	15.35	5.89	77.33	29.63	131.56	31.64	355.30	69.19	3.56	9017.08	173.44	81.75	0.13	78.64	0.16	55.63	−17.84	658
LQL12-7-15-04	0.16	8.63	0.10	1.43	2.70	0.33	16.93	6.49	85.56	32.79	144.08	35.75	406.82	75.97	8.18	8821.08	190.06	95.75	1.19	59.50	0.15	43.65	−15.05	724
LQL12-7-15-05	0.10	8.18	0.06	0.75	2.89	0.52	16.39	6.80	92.86	37.42	168.06	42.92	522.66	96.92	9.09	9186.07	277.09	83.75	3.60	115.37	0.23	77.64	−12.42	733
LQL12-7-15-06	0.10	9.04	0.07	1.48	2.81	0.92	20.67	7.84	102.93	39.08	174.43	41.22	468.52	88.65	7.87	8324.85	213.47	148.42	1.17	61.79	0.37	44.52	−15.15	720
LQL12-7-15-07	0.07	9.91	0.13	3.55	8.06	1.01	44.72	16.16	184.28	68.94	291.33	65.87	732.30	133.76	3.76	8955.20	230.54	146.59	−4.81	18.38	0.16	14.43	−22.67	662
LQL12-7-15-08	0.12	16.21	0.16	3.30	8.05	2.24	48.36	18.42	245.40	94.10	406.65	93.71	1062.49	192.63	11.18	7219.06	360.02	300.48	0.63	42.58	0.35	30.96	−14.95	751
LQL12-7-15-09	0.14	8.56	0.13	0.92	2.41	0.45	19.93	8.06	105.01	41.37	186.07	45.98	519.29	100.28	5.75	9183.97	190.58	92.91	2.21	105.98	0.20	71.50	−14.76	695
LQL12-7-15-10	2.95	16.21	0.93	5.60	4.67	0.55	19.71	7.50	95.39	37.83	165.23	41.26	463.56	85.12	5.63	9693.69	223.09	116.66	−2.20	26.24	0.18	22.41	−19.22	693
LQL12-7-15-11	0.05	7.55	0.08	1.51	3.13	0.74	16.52	6.72	86.16	34.36	162.08	41.20	488.31	95.34	7.37	8318.88	270.86	134.70	0.53	53.32	0.32	39.13	−15.92	715
LQL12-7-15-12	0.15	7.55	0.10	1.63	3.82	0.51	20.08	8.18	102.51	39.02	172.34	42.42	467.00	86.94	5.54	8920.12	168.51	85.14	−1.19	39.99	0.18	29.61	−18.24	692
LQL12-7-15-13	0.09	11.40	0.10	0.99	2.99	0.38	18.51	7.72	103.17	41.81	195.03	50.06	592.75	114.58	3.69	9759.02	410.41	251.59	2.05	133.36	0.16	90.63	−15.85	660
LQL12-7-15-15	0.08	9.13	0.10	0.92	2.55	0.44	17.02	6.76	85.39	34.72	158.68	38.68	432.25	82.80	4.15	9326.30	219.19	93.34	1.36	101.25	0.20	70.07	−16.29	669
LQL12-7-15-16	0.47	8.67	0.20	2.15	2.89	0.40	15.71	6.55	88.02	35.22	159.27	38.75	447.18	87.90	3.93	9256.60	162.07	72.40	−1.45	45.02	0.18	34.28	−19.22	665
LQL12-7-15-17	0.39	7.91	0.13	1.56	3.55	0.51	21.07	7.97	102.44	38.89	172.59	42.79	474.70	90.71	4.27	9035.94	153.41	73.01	−1.34	45.77	0.18	33.55	−18.93	671
LQL12-7-15-18	0.05	8.55	0.07	1.16	3.37	0.56	22.43	9.00	115.74	43.99	191.70	45.85	513.76	97.27	4.01	9363.67	181.75	96.68	−0.19	68.04	0.20	47.43	−17.91	667
LQL12-7-15-19	0.11	11.15	0.12	3.53	9.63	1.66	46.18	16.87	201.74	74.61	310.22	71.53	782.19	141.80	4.37	9120.06	255.39	179.04	−4.22	19.73	0.24	15.37	−21.76	673
LQL12-7-15-20	0.09	9.28	0.08	1.64	4.96	1.16	29.10	11.14	143.87	55.78	244.85	58.34	639.54	123.96	6.56	8494.44	195.44	126.73	−0.21	48.57	0.30	34.59	−16.91	705
LQL12-7-15-21	0.05	8.82	0.05	0.96	2.79	0.34	16.78	6.78	86.78	33.79	150.62	36.43	413.97	79.32	8.68	10100.02	185.77	93.29	2.57	86.72	0.15	60.74	−13.54	729
Granite porphyry																								
LQL13-3-37-4-2	0.02	11.52	0.09	1.67	4.03	1.25	27.55	10.48	137.88	56.38	266.19	57.24	548.01	113.34	13.31	8243.78	302.47	235.53	2.50	65.99	0.36	45.56	−12.72	767
LQL13-3-37-4-3	1.67	22.89	0.72	5.72	8.77	1.73	52.58	19.88	236.91	90.40	406.71	84.32	793.95	157.79	17.37	8854.66	502.01	351.25	0.57	30.16	0.25	23.06	−14.09	792
LQL13-3-37-4-5	0.07	10.77	0.07	1.72	3.64	0.64	23.06	8.09	103.72	40.72	187.19	40.51	371.74	76.66	2.46	8550.02	295.60	181.87	−2.30	50.73	0.21	36.68	−21.05	631
LQL13-3-37-4-6	0.02	8.61	0.27	4.99	11.75	3.10	61.72	20.49	237.00	88.63	374.66	73.17	658.85	129.58	3.86	7379.06	249.33	173.29	−7.47	8.41	0.35	7.00	−25.27	664
LQL13-3-37-4-7	0.00	15.24	0.05	1.36	3.83	0.39	22.26	8.72	114.00	45.62	213.38	45.37	427.14	84.13	3.27	10944.11	394.97	195.44	0.57	95.27	0.13	65.87	−17.59	651
LQL13-3-37-4-8	0.04	12.97	0.09	2.02	4.18	1.13	29.08	11.50	149.11	62.28	294.34	63.17	584.97	123.59	4.95	8156.05	289.36	157.97	0.10	64.50	0.31	44.87	−17.18	683
LQL13-3-37-4-10	5.30	25.53	1.95	13.61	13.41	2.78	65.60	21.73	249.89	93.77	400.34	81.64	745.48	142.43	6.92	8472.58	344.89	230.28	−4.97	10.56	0.29	9.42	−21.55	710
LQL13-3-37-4-11	0.91	16.95	0.31	2.46	3.19	0.33	21.34	7.85	103.17	41.47	188.82	60.80	371.23	73.19	3.50	10206.10	395.26	211.03	−0.52	63.69	0.12	47.29	−18.53	656
LQL13-3-37-4-12	0.23	20.77	0.16	3.22	5.35	0.82	36.89	13.47	167.18	66.57	297.78	60.10	559.51	111.69	2.68	9742.63	471.12	280.09	−1.92	52.61	0.18	38.55	−20.49	637
LQL13-3-37-4-13	0.40	14.62	0.18	1.70	3.87	0.35	22.20	7.69	98.02	39.12	188.12	39.62	372.04	75.87	3.13	9893.06	365.65	169.65	−0.61	68.61	0.12	49.56	−18.85	648
LQL13-3-37-4-14	0.31	14.78	0.37	5.90	12.74	3.15	73.81	25.31	298.10	110.91	485.96	96.98	877.52	169.09	1.94	8343.96	409.24	293.92	−7.27	14.46	0.31	11.35	−26.51	615
LQL13-3-37-4-15	0.01	13.02	0.08	2.20	5.27	1.37	34.67	12.89	167.99	68.66	316.29	66.98	631.88	128.07	4.05	8347.91	318.34	162.12	−1.15	52.07	0.31	36.53	−18.85	667
LQL13-3-37-4-16	0.05	15.95	0.09	1.65	4.92	0.73	31.63	11.40	148.56	59.74	281.45	60.10	564.04	113.69	5.64	9447.23	381.42	221.65	1.23	81.23	0.18	55.80	−15.78	693
LQL13-3-37-4-17	0.34	14.49	0.16	1.52	2.87	0.47	20.03	7.60	99.19	40.25	183.94	39.60	362.67	73.26	3.13	10019.90	357.25	177.72	−0.97	89.07	0.19	62.85	−20.32	611
LQL13-3-37-4-18	0.08	16.53	0.12	1.30	4.64	0.64	30.28	11.24	148.63	59.93	279.00	58.70	558.80	111.17	9.15	10096.34	381.54	150.69	3.31	106.91	0.17	71.52	−12.69	733
LQL13-3-37-4-19	1.30	12.27	0.53	4.79	6.40	2.05	36.36	13.39	160.77	66.20	305.39	64.34	616.46	125.19	6.45	7722.94	243.69	150.69	−3.03	21.03	0.41	16.51	−19.76	704
LQL13-3-37-4-20	0.08	12.01	0.01	0.79	3.12	0.35	18.44	6.79	90.28	37.15	174.49	36.83	356.73	71.54	4.27	9798.64	317.25	144.95	2.13	126.67	0.14	84.60	−15.46	671

Table 5 (*continued*)

Sample spot	La	Ce	Pr	Nd	Sm	Eu	Gd	Tb	Dy	Ho	Er	Tm	Yb	Lu	Ti	Hf	U	Th	ΔFMQ*	Ce^{4+}/Ce^{3+}	$Eu_N/Eu_N{}^*$	δCe	$lg(fO_2)$	T (°C)
LQL13-3-37-4-21	0.12	13.70	0.23	4.46	7.28	2.03	44.17	14.71	178.07	69.90	312.90	64.98	606.66	119.14	5.89	8508.08	290.99	219.35	−3.19	21.52	0.35	16.74	−20.12	696
LQL13-3-37-4-23	1.79	17.59	0.66	4.70	5.50	0.89	29.64	10.57	132.13	53.60	248.96	53.77	512.09	103.86	8.01	8565.89	304.99	156.13	−0.96	31.70	0.21	24.97	−17.24	722
LQL13-3-37-4-24	0.00	10.57	0.05	1.68	4.45	1.03	27.67	10.68	142.33	60.01	290.00	62.70	586.20	122.21	9.97	8164.72	293.44	142.95	1.50	60.96	0.28	41.92	−14.32	741
LQL13-3-37-4-25	0.01	9.62	0.11	1.98	4.16	1.57	31.00	11.53	154.65	64.09	304.43	64.99	622.80	129.63	5.73	7808.68	260.46	129.62	−0.55	49.58	0.42	34.44	−17.53	694

Notes: ΔFMQ* are calculated by the method from Trail et al. (2011) and Qiu et al. (2013).

granodiorites (ε$_{Hf(t)}$ values range from +2.5 to +8.4) (Fig. 11B). Thus, the only rational mechanism for petrogenesis of the Jubuzhari complex might be the partial melting of mafic to intermediate *meta*-igneous crustal rocks, which is agreement with the isotopic data discussed below.

High SiO$_2$ and total REEs (Figs. 8A; 10A) (higher than basaltic rocks in composition), and are enriched in large-ion lithophile elements (Rb, Pb, and K) and relatively depleted in high-field strength elements (Ta, Ti, and Nb) (Fig. 10B) indicate that crustal rocks should have played an important role in the generation of the Jubuzhari complex intrusions (Green, 1995; Hofmann et al., 1986; Prouteau et al., 1999; Rushmer, 2001; Wedepohl, 1995). Zhu et al. (2011) have pointed that the central Lhasa subterrane is unique with ancient crustal base. The negative ε$_{Hf(t)}$ values of −6.3, with an old Hf model ages (1522 Ma) appeared in the granodiorite porphyry, suggests the involvement of ancient central Lhasa basement-derived melts in the generation of Jubuzhari complex. However, the Hf isotope data in the Jubuzhari complex intrusions are mainly characterized by positive ε$_{Hf(t)}$ values (+1.3 to +8.4) and young Hf model ages (599–1045 Ma) (Fig. 11), which could not be explained by partial melting of the ancient crustal base, indicating that a great deal of mantle materials have involved in the generation of Jubuzhari complex. Hence, the Jubuzhari complex intrusions are mainly from a mantle-crust mixed source, which is likely the juvenile crust of the southern Lhasa subterrane, partial melting of such crust materials will produce magmas (i.e. the Gangdese Batholith) showing juvenile zircon ε$_{Hf(t)}$ values (mostly +5 to +10) (Chung et al., 2009; Hou et al., 2013; Ji et al., 2009; Li et al., 2011; Zhu et al., 2011). Nevertheless, it should be noted that the Jubuzhari complex intrusions have a certain amount of low zircon ε$_{Hf(t)}$ values (+1 to +5) compared with the Gangdese Batholith (Fig. 11B–D), indicating that the influence of mantle materials in this area is less than in the southern Lhasa subterrane or the crustal base is not that juvenile than the southern Lhasa subterrane (Chu et al., 2006; Chung et al., 2005; Zhu et al., 2011). In this case, the crust nature of this area is different from the juvenile crust, so we preliminary define the magma origin into a 'reworking' crust. In summary, the Jubuzhari complex intrusions were most likely derived from partial melting of a 'reworking' crust, mixed with the ancient central Lhasa basement and a great deal of mantle materials.

6.2.2. Evolution of the ore-forming rocks

Contents of CaO, Al$_2$O$_3$, MgO, Fe$_2$O$_3$, P$_2$O$_5$, TiO$_2$ of granodiorite, granodiorite porphyry and granite porphyry show negative correlations with SiO$_2$ (Fig. 9), all rock types have similar REEs and trace-element distributions (Fig. 10), and zircon Hf isotopic compositions (Fig. 11), indicating a close genetic relationship. The granodiorite porphyry and granite porphyry have high DI of 89–90 and 93–94 (Fig. 8D), and enhanced (Na$_2$O + K$_2$O)/CaO and FeO*/MgO ratios (Fig. 14A, B), suggesting that they had undergone extensive fractionation (Whalen et al., 1987). Negative correlations between Sr and Ba (Fig. 14C) and between Sr and Rb/Sr (Fig. 14D) could be interpreted as the consequences of fractional crystallization of plagioclase (or K-feldspar) and hornblende. However, fractional crystallization of K-feldspar might not be the control factor for the content of Sr and Ba, because contents of K$_2$O decrease with increasing of SiO$_2$ contents (Table 3; Fig. 8B). This is consistent with the petrographically observations of granite porphyries that show more abundant K-feldspar megacrysts and less plagioclase ± hornblende comparing with those of granodiorite porphyries and granodiorites. For example, the Ba, Sr, and Rb abundances of granite porphyries can be quantitatively explained by 30–60 % fractionation of 70% plagioclase and 30% hornblende starting from the assumed parent magma composition represented by the less fractionated sample (LQL13-4-5-1) of granodiorite (Fig. 14C, D). The explanation is also supported by the negative Eu depletions (e.g. Hanson, 1978; Richards and Kerrich, 2007), and the absence of a negative trend between SiO$_2$ and Sc (Fig. 14E), which is expected in hornblende
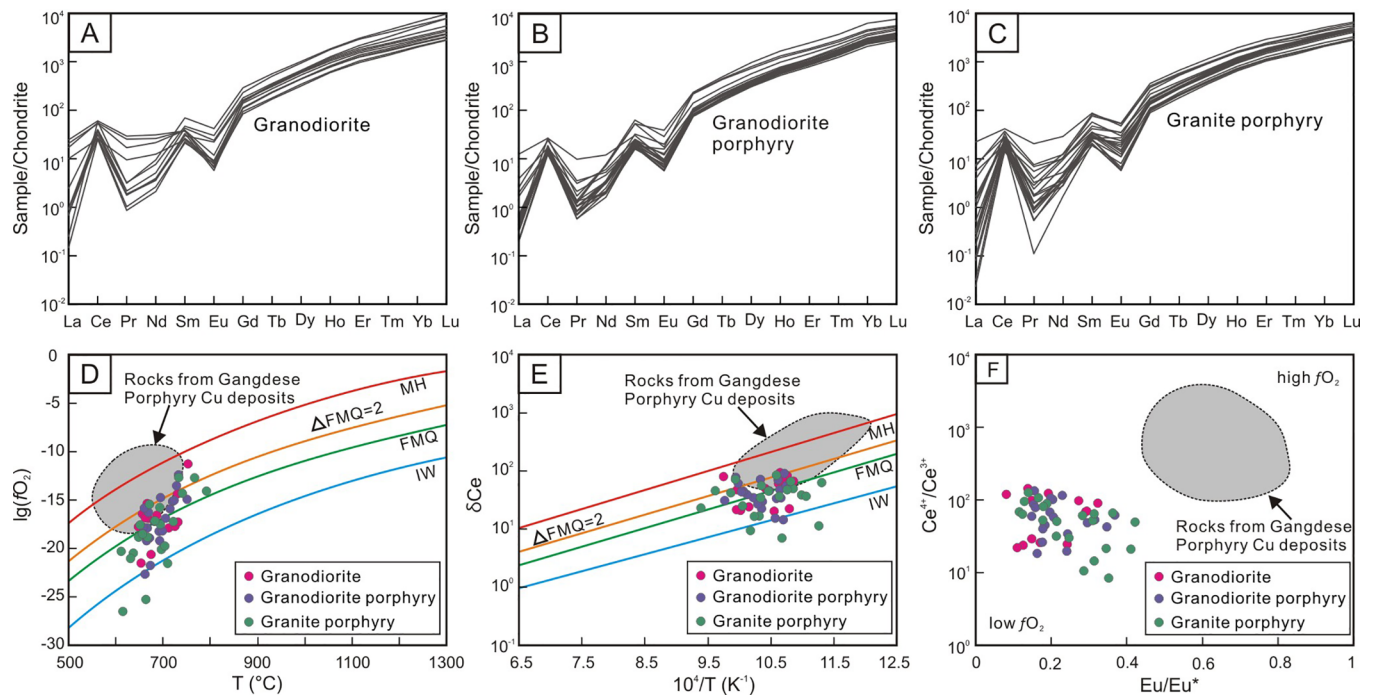
Fig. 12. A–C) Chondrite-normalized REE patterns for zircons from the ore-forming rocks in the Lietinggang-Leqingla deposit; D) Zircon fO_2 versus temperature histogram of Lietinggang-Leqingla deposit; E) Zircon Magma oxidation states of Lietinggang-Leqingla deposit; F) Zircon Ce^{4+}/Ce^{3+} ratios versus Eu_N/Eu_N* showing the magma oxidation states. Normalization values and Eu_N/Eu_N* ratios are from Sun and McDonough (1989); Temperature is calculated from Watson et al. (2006) and Ferry and Watson, (2007); the calculation of zircon Ce^{4+}/Ce^{3+} ratios and ΔFMQ values are based on Ballard et al. (2002) and Qiu et al. (2013). The data of rocks from Gangdese porphyry Cu deposits are from Zheng et al. unpublished data.

controlled fractionation (Davidson et al., 2007). Biotite is enriched in V element and relatively depleted in Th element, and hence the negative trend between V and Th (Fig. 14F), indicates that the biotite has experienced fractionation (Bea et al., 1994), which is consistent with the fact that the biotite content of the samples are decrease gradually from the granodiorites to the granite porphyries.

Negative Nb, Ta, Ti and P anomalies (Fig. 10B) are commonly attributed to the fractionation of ilmenite and/or titanite, and apatite. Nb/Ta ratio of igneous rocks is mainly controlled by (1) fractionation of ilmenite and rutile, which will cause the ratio increasing (Linnen and Keppler, 1997), (2) fractionation of low-magnesium hornblende or biotite, which will cause the ratio decreasing (Pfänder et al., 2007; Stepanov and Hermann, 2013), and (3) injection of fluorine-enrichment fluid, which will cause the ratio increasing (Anderson et al., 2013). In the Nb/Ta vs. Zr/Hf diagram (Fig. 14G), the decrease of Nb/Ta ratio from granodiorite to granite porphyry though granodiorite porphyry suggests that hornblende/biotite underwent fractionation during the magma evolution or fluorine-enrichment fluid injected into the magma system. No fluorine-enrichment minerals (such as fluorite and fluorspar) has been found in magmas in the Lietinggang-Leqingla mining district, indicating that the decrease of Nb/Ta ratio should be caused by fractionation of low-magnesium hornblende and/or biotite. The decrease of Zr/Hf ratio should be influenced by fractionation of zircon (Fig. 14G) (Linnen and Keppler, 2002).

In summary, major and trace elements and zircon Hf isotope data indicate that the ore-forming intrusions of the Lietinggang-Leqingla deposit contain moderately and strongly fractionated I-type granite. These intrusions were mainly derived from partial melting of a 'reworking' crust, mixed with the ancient central Lhasa basement and a great deal of mantle materials. The granodiorite porphyry and granite porphyry were most likely derived from the melts represented by granodiorite through fractional crystallization of plagioclase, hornblende, biotite, ilmenite, titanite, apatite, and zircon.

6.3. Factors controlling the polymetallic mineralization

Previously studies have indicated that the Gangdese porphyry Cu–(Mo) deposits are associated with the juvenile materials (e.g. Hou et al., 2013, 2015b; Li et al., 2011; Yang et al., 2016). Metasomatized lithospheric mantle was critical for the development of the Cu-Mo-Au deposits, while partial melting of ancient crust was the key source material for Pb–Zn mineralization (Zheng et al., 2015). The ore-forming intrusions of Lietinggang-Leqingla deposit are mainly derived from a mantle-crust mixed source (Fig. 11). It seems that the magma source of Lietinggang-Leqingla deposit have the potential of generation Fe–Cu and Pb–Zn mineralization.

Iron is strongly compatible element in mineral phases, which is typically enriched in the mantle (Hofmann, 1988; Gao et al., 1998). Thus, the involvement of mantle materials in the genesis of magmas is benefit to Fe mineralization. Similar to other skarn Fe deposits in the world (Meinert, 1992), ore-forming rocks related to the skarn Fe deposits in the Lhasa terrane are also characterized by calc-alkaline and metaluminous compositions, high in compatible elements. These magmas commonly have high volumes of iron-bearing hornblende and biotite. Breaking down of these iron-bearing minerals during hydrothermal alteration can contribute iron to skarn Fe mineralization.

Copper is incompatible in an oxidized melt but compatible under relatively reducing conditions (Richards, 2009; Wang et al., 2014c). Many researches have been paid for association between magmatic oxygen fugacity and the porphyry Cu–(Au) mineralization. Cu and Au are chalcophile elements, with high partition coefficients between sulfide and melts. Li and Audétat (2015) further implies that sulfide liquid saturation in low-temperature intermediate to felsic melts causes a strong depletion in Cu, and Au in the silicate melt, whereas mono-sulfide solid solution saturation may cause depletion in Cu and potentially Au. Thus, the behaviors of these elements are mainly controlled by the oxidation state of sulfur in a melt (Mungall and Brenan, 2014). Under more oxidizing conditions (and more hydrous) magmagenesis, residual
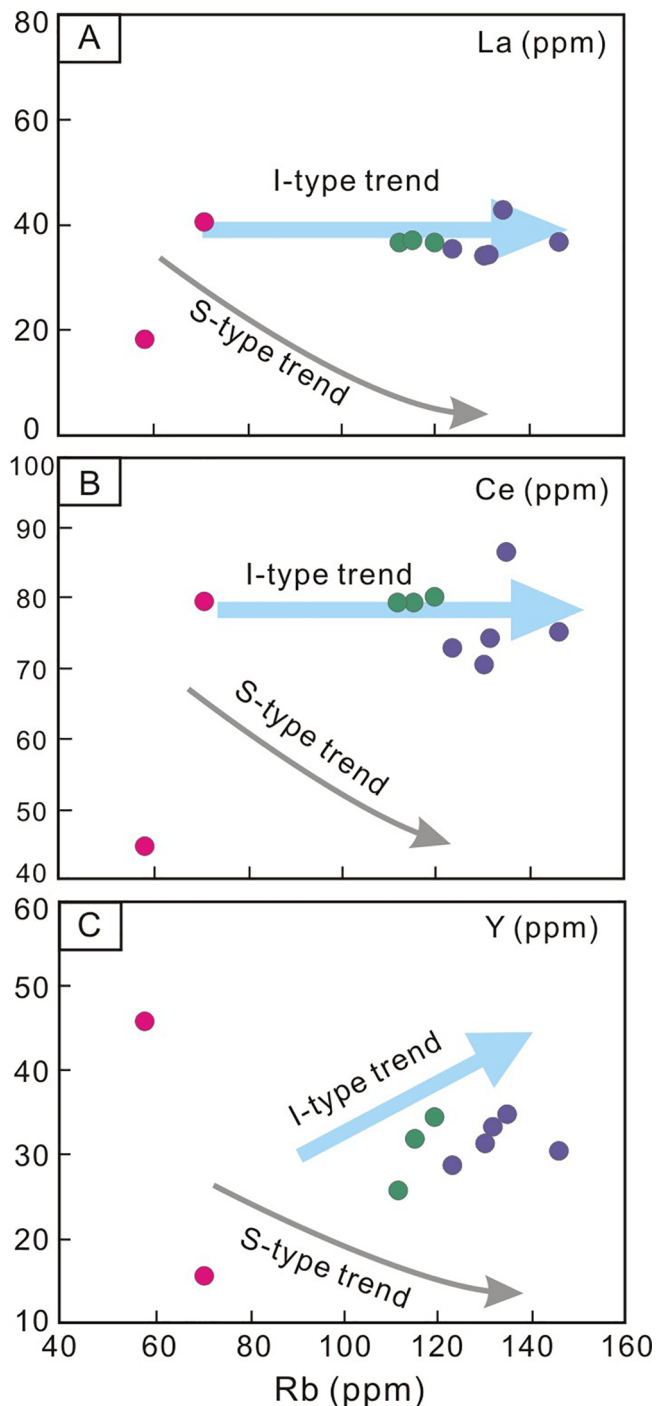
Fig. 13. Plots of La, Ce and Y versus Rb showing evolution trends of I-type and S-type magmas in the ore-forming rocks from the Lietinggang-Leqingla deposit.

sulfides from prior arc magmatism in the mantle or deep crust may have been remobilized, releasing Cu and Au into the melts and thus making them available for later magmatic-hydrothermal mineralization upon emplacement in the upper crust (Richards, 2009, 2011; Chiaradia, 2014; Wang et al., 2014c). The fO_2 indicators of Lietinggang-Leqingla deposit suggest these magmas were weakly oxidized to moderately reduced, with mostly ΔFMQ $<$ $+2.0$ (Fig. 12D, E). Under reduced conditions, sulfide saturation will strip Cu from the melt, and leave residual sulfide phases as restite in the mantle or as cumulate minerals in the deep crust during fractionation and crustal interaction (i.e., in the MASH zone of Richards, 2009, 2011; Chiaradia, 2014). Consequently, the less oxidized Lietinggang-Leqingla magmas may have left much of

their metal load in the mantle or lower crust, leading to sparse upper crustal Cu mineralization. Thus, the scale of Cu mineralizaiton in the Lietinggang-Leqingla deposit is much less than that of the Miocene porphyry Cu deposits in the Lhasa terrane. Additionally, combined with the presence of high ΔFMQ values (up to 4.3), relatively higher average ΔFMQ values of Lietinggang-Leqingla magmas than that of the Paleocene–Eocene unmineralized magmas (ranging from -1.2 to 0.8) (Wang et al., 2014c) could be the reason why the Lietinggang-Leqingla deposit still has some degree of Cu mineralization.

Pb and Zn are geochemically similar and are common elements in the mineral assemblages of ore deposits. Pb is strongly incompatible in mineral phases and typically enriched in the upper continental crust due to crust–mantle formation (Hofmann, 1988; Gao et al., 1998). The central Lhasa subterrane is unique with ancient crustal base (Zhu et al., 2011), with relative high Pb content (Wu et al., 2003b), and the ancient central Lhasa basement-derived melts involved in the generation of the ore-forming intrusions of Lietinggang-Leqingla deposit. Therefore, partial melting of the ancient crust would supply much Pb and Zn to the melts, which is available for the Pb–Zn mineralization. Furthermore, most of the ore-forming rocks from Pb–Zn deposits in the Lhasa terrane had undergone more extensive fractionation than Fe–Cu deposits (Fig. 14A, B). The Pb content was increasing with the magmatic evolution (DI < 90) (Fig. 14H), indicating Pb was enriched throughout magmatic evolution (Stanton, 1994). However, as the continuous magmatic evolution (DI > 90), the Pb content in magmas decreased (Fig. 14H), which might mean that Pb had been transferred to fluid for further magmatic evolution. Li and Audétat (2015) implies that Pb and Zn are much less or not affected by the saturation of sulfide liquid or monosulfide solid solution. Therefore, it seems that the magmatic oxygen fugacity may have no influence to the Pb–Zn mineralization in Lietinggang-Leqingla deposit. In general, the Pb–Zn mineralization in the Lhasa terrane was controlled by the initial enrichment of metal in the source region and subsequent extensive fractionation processes.

6.4. Implication for the evolution of regional Fe–Cu–Pb–Zn mineralization

Combined with existing data, we summarize the geodynamic setting of the Fe–Cu–Pb–Zn mineralization in the Lhasa terrane (Fig. 15). The Indian–Asian continental collision may not only have thickened the Lhasa lithosphere, but also induced roll-back of the flat-subducting Neo–Tethyan oceanic slab. The process of oceanic slab roll-back could greatly enhance the asthenospheric corner flow or partial melting of mantle wedge (Chung et al., 2005; Mo et al., 2007; Wen et al., 2008). Heat transfer from the hot asthenosphere will increase the geothermal gradient in the lithosphere. In this model, the magmas related to Fe–Cu ore-forming intrusions would have been derived from partial melts of the metasomatized lithospheric mantle beneath the central Lhasa subterrane (Zheng et al., 2015). Furthermore, these mantle-derived melts stored at the base of the crust and mixed with the ancient central Lhasa subterrane crustal melts (Zhu et al., 2011), forming a 'reworking' crust. The magmas derived from partial melting of the 'reworking' crust, underwent extensive fractional crystallization processes during the ascent and emplacement is critical to Fe–Cu–Pb–Zn polymetallic mineralization. Subsequently, the ascent and emplacement of mantle- and 'reworking' crust- derived melts into shallow crustal levels would have induced partial melting of the middle–upper ancient crust, forming Pb–Zn deposits (Zheng et al., 2015).

7. Conclusions

The data presented in this article, combined with the findings of earlier published work, lead us to conclude the petrogenesis and metallogenesis of the Lietinggang-Leqingla skarn type Fe–Cu–(Mo)–Pb–Zn deposit in the Lhasa terrane. Our key conclusions are summarized as follows:
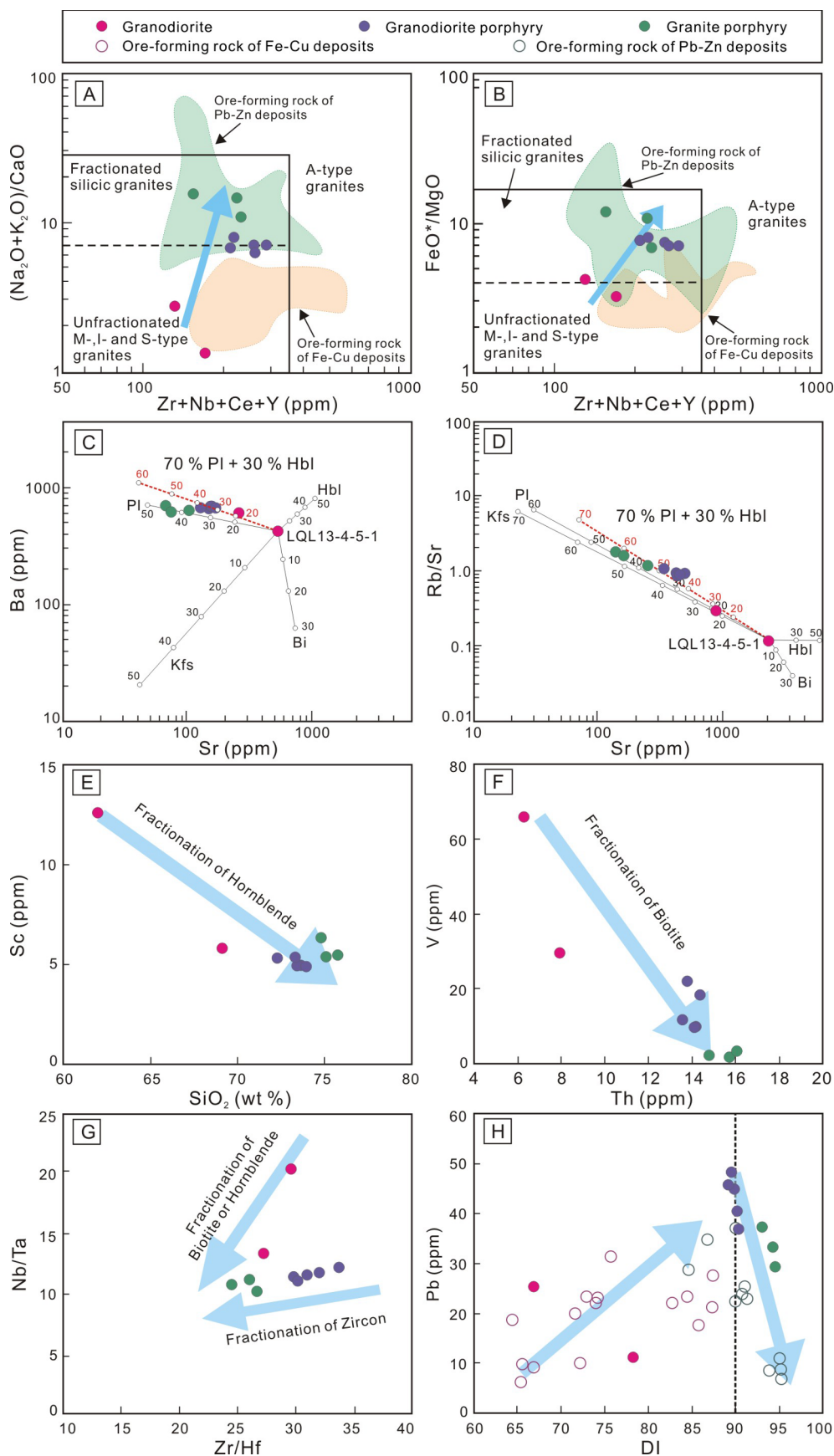
Fig. 14. A) (Na₂O + K₂O)/CaO versus (Zr + Nb + Ce + Y) and B) FeO*/MgO versus (Zr + Nb + Ce + Y) plots (Whalen et al., 1987) of the ore-forming rocks from the Lietinggang-Leqingla deposit; C) Ba versus Sr and D) Rb/Sr versus Sr plots showing fractionation of plagioclase and hornblende which controlled the variation of these elements from granodiorite to granodiorite porphyry, and to granite porphyry samples; E) The absence of a negative trend between SiO₂ and Sc, showing fractionation of hornblende; F) V versus Th plots showing fractionation of biotite; G) Nb/Ta versus Zr/Hf plots showing fractionation of hornblende, biotit and zircon; H) Pb versus DI plots. Data of ore-forming rock of Fe–Cu deposits from Fu et al. (2013) and Zheng et al. (2015); Data of ore-forming rock of Pb–Zn deposits from Zheng et al. (2015) and Fu et al. (2017). Partition coefficients are from Rollinson. (1993), Green and Pearson. (1986), Mahood and Hildreth. (1983), and Yurimoto et al. (1990).
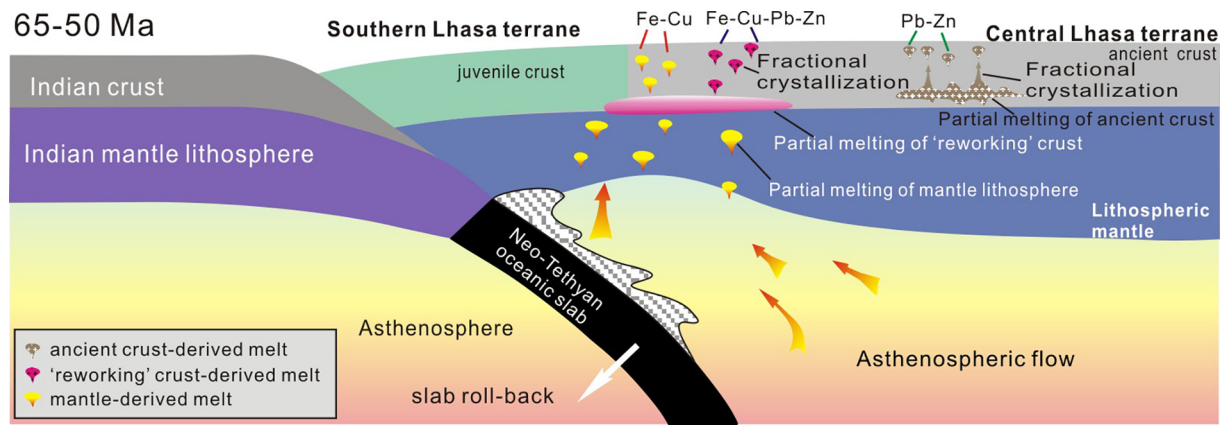
Fig. 15. Proposed tectonic illustrations of the development of the Fu–Cu–Pb–Zn mineralization in the central Lhasa subterrane. Modified from Chung et al. (2005), Fu et al. (2017), Hou et al. (2006a), and Zheng et al. (2015).

(1) The ore-forming rocks of the Lietinggang-Leqingla deposit are composed of granodiorite (formed at 62.4 ± 1.2 Ma), granodiorite porphyry (formed at 62.6 ± 0.6 Ma) and granite porphyry of 63.7 ± 1.0 Ma. Molybdenite yield a Re–Os isochron age of 59.0 ± 1.7 Ma. The almost identical ages constraints between the intrusions and mineralization indicate that the intrusions and the mineralization are genetically coeval, and occurred during or shortly before the main stage of the Indian–Asian continental collision.

(2) The ore-forming intrusions include moderately (granodiorite) and strongly (granodiorite porphyry and granite porphyry) fractionated I-type granites, which were mainly derived from partial melting of a 'reworking' crust, mixed with the ancient central Lhasa basement and a great deal of mantle materials.

(3) The granodiorite porphyry and granite porphyry were most likely derived from the melts represented by granodiorite through fractional crystallization of plagioclase, hornblende, biotite, ilmenite, titanite, apatite, and zircon.

(4) The oxidation state of Lietinggang-Leqingla magmas was weakly oxidized to moderately reduced, which caused Lietinggang-Leqingla deposit had some degree of Cu mineralization, but much less than that of the Miocene porphyry Cu deposits in the Lhasa terrane.

(5) The magmas source, magmatic fractional crystallization and oxidation state of magmas could influence the Fe–Cu–Pb–Zn poly-metallic mineralization in the Lhasa terrane.

Acknowledgements

References

Andersen, T., 2002. Correction of common lead in U-Pb analyses that do not report [204]Pb. Chem. Geol. 192, 59–79.

Anderson, M.O., Lentz, D.R., McFarlane, C.R., Falck, H., 2013. A geological, geochemical and textural study of an LCT pegmatite: implications for the magmatic versus metasomatic origin of Nb–Ta mineralization in the Moose II pegmatite, Northwest Territories, Canada. J. Geosci. 58, 299–320.

Bacon, C., Druitt, T., 1988. Compositional evolution of the zoned calcalkaline magma chamber of Mount Mazama, Crater Lake, Oregon. Contrib. Miner. Petrol. 98, 224–256.

Ballard, J.R., Palin, J.M., Campbell, I.H., 2002. Relative oxidation states of magmas inferred from Ce(IV)/Ce(III) in zircon: application to porphyry copper deposits of northern Chile. Contrib. Miner. Petrol. 144, 347–364.

Bea, F., Pereira, M.D., Stroh, A., 1994. Mineral/leucosome trace-element partitioning in a peraluminous migmatite (a laser ablation-ICP-MS study). Chem. Geol. 117, 291–312.

Beard, J.S., Lofgren, G.E., 1991. Dehydrationmelting and water-saturated melting of basaltic and andesitic greenstones and amphibolites at 1, 3, and 6.9 kb. J. Petrol. 32, 365–401.

Black, L.P., Kamo, S.L., Williams, I.S., Mundil, R., Davis, D.W., Korsch, R.J., Foudoulis, C., 2003. The application of SHRIMP to phanerozoic geochronology: a critical appraisal of four zircon standards. Chem. Geol. 200, 171–188.

Blisniuk, P.M., Hacker, B., Glodny, J., Ratschbacher, L., Bill, S., Wu, Z.H., McWilliams, M.O., Calvert, A., 2001. Normal faulting in central Tibet since at least 13.5 Myr ago. Nature 412, 628–632.

Blundy, J., Wood, B., 1994. Prediction of crystal-melt partition coefficients from elastic moduli. Nature 372, 452–454.

Chappell, B.W., 1999. Aluminium saturation in I- and S-type granites and the characterization of fractionated haplogranites. Lithos 46, 535–551.

Chappell, B.W., Stephens, W.E., 1988. Origin of infracrustal (I-type) granite magmas. Trans. R. Soc. Edinburgh Earth Sci. 79, 71–86.

Chappell, B.W., White, A.J.R., 1974. Two contrasting granite types. Pac. Geol. 8, 173–174.

Chappell, B.W., White, A.J.R., 1992. I- and S-type granites in the Lachlan Fold Belt. Geol. Soc. Am. Spec. Papers 272, 1–26.

Chappell, B.W., White, A.J.R., 2001. Two contrasting granite types: 25 years later. Aust. J. Earth Sci. 48, 489–499.

Chiaradia, M., 2009. Adakite-like magmas from fractional crystallization and melting-assimilation of mafic lower crust (Eocene Macuchi arc, Western Cordillera, Ecuador). Chem. Geol. 265, 468–487.

Chiaradia, M., 2014. Copper enrichment in arc magmas controlled by overriding plate thickness. Nat. Geosci. 7, 43–46.

Chu, M.F., Chung, S.L., Song, B., Liu, D.Y., O'Reilly, S.Y., Pearson, N.J., Ji, J.Q., Wen, D.J., 2006. Zircon U-Pb and Hf isotope constraints on the Mesozoic tectonics and crustal evolution of southern Tibet. Geology 34, 745–748.

Chung, S.L., Chu, M.F., Zhang, Y.Q., Xie, Y.W., Lo, C.H., Lee, T.Y., Lan, C.Y., Li, X.H., Zhang, Q., Wang, Y.Z., 2005. Tibetan tectonic evolution inferred from spatial and temporal variations in post-collisional magmatism. Earth Sci. Rev. 68, 173–196.

Chung, S.L., Chu, M.F., Ji, J.Q., O'Reilly, S.Y., Pearson, N.J., Liu, D.Y., Lee, T.Y., Lo, C.H., 2009. The nature and timing of crustal thickening in southern Tibet. Tectonophysics 477, 36–48.

Coleman, M., Hodges, K., 1995. Evidence for Tibetan Plateau uplift before 14 Ma ago from a new minimum age for east-west extension. Nature 374, 49–52.

Collins, W.J., Richards, S.W., 2008. Geodynamic significance of S-type granites in circum-Pacific orogens. Geology 36, 559–562.

Davidson, J., Turner, S., Handley, H., Macpherson, C., Dosseto, A., 2007. Amphibole "sponge" in arc crust? Geology 35, 787–790.

Davis, D.W., Amelin, Y., Nowell, G.M., Parrish, R.R., 2005. Hf isotopes in zircon from the western Superior province, Canada, implications for Archean crustal development and evolution of the depleted mantle reservoir. Precambr. Res. 140, 132–156.

Deng, J., Wang, Q.F., Li, G.J., Santoh, M., 2014. Cenozoic tectono-magmatic and metallogenic processes in the Sanjiang region, southwestern China. Earth Sci. Rev. 138, 26–299.

Deng, J., Wang, C.M., Zi, J.W., Xia, R., Li, Q., 2018. Constraining subduction-collision processes of the Paleo-Tethys along the Changning-Menglian Suture: new zircon U-Pb ages and Sr–Nd–Pb–Hf–O isotopes of the Lincang Batholith. Gondwana Res. 62, 75–92.

Ding, L., Lai, C., 2003. Geologic evidence for preexisting crustal thickening and uplift in the Lhasa terrane before the Indo-Asian collision. Chin. Sci. Bull. 48, 836–842.

Ding, L., Maksatbek, S., Cai, F.L., Wang, H.Q., Song, P.P., Ji, W.Q., Xu, Q., Zhang, L.Y., Muhammad, Q., Upendra, B., 2017. Processes of initial collision and suturing between India and Asia. Sci. China Earth Sci. 47, 293–309.

Du, A.D., Wu, S.Q., Sun, D.Z., Wang, S.X., Qu, W.J., Markey, R., Stein, H., Morgan, J., Malinovskiy, D., 2004. Preparation and certification of Re-Os dating reference materials: molybdenite HLP and JDC. Geostand. Geoanal. Res. 28, 41–52.

Dürr, S., 1996. Provenance of Xigaze forearc clastic rocks (Cretaceous, south Tibet). Geol. Soc. Am. Bull. 108, 669–691.

Ferry, J.M., Watson, E.B., 2007. New thermodynamic models and revised calibrations for the Ti-in-zircon and Zr-in-rutile thermometers. Contrib. Miner. Petrol. 154, 429–437.

Fu, Q., Zheng, Y.C., Huang, K.X., 2012. Sulfur and lead isotopic composition of Longmala polymetallic deposit, Tibet and its geological significance. Nonferrous Met. (Min. Sect.) 64, 26–30 (in Chinese with English abstract).

Fu, Q., Yang, Z.S., Zheng, Y.C., Huang, K.X., Li, Q.Y., Li, W., Liang, W., Sun, Q.Z., Zhang, S., 2013. Zircon U-Pb ages, Hf isotope and geochemistry of granodiorite in Jialapu Fe deposit, Tibet. Min. Deposits 32, 564–578 (in Chinese with English abstract).

Fu, Q., Yang, Z.S., Zheng, Y.C., Huang, K.X., Duan, L.F., 2014. Ar–Ar age of phlogopite from Longmala copper–iron–lead–zinc deposit in Tibet, and its geodynamic significance. Acta Petrol. Mineral. 33, 283–293 (in Chinese with English abstract).

Fu, Q., Huang, K.X., Zheng, Y.C., Yang, Z.S., Duan, L.F., 2015. Ar–Ar Age of muscovite from skarn orebody of the MengYa'a lead–zinc Deposit in Tibet, and its geodynamic significance. Acta Geol. Sin. 89, 569–582 (in Chinese with English abstract).

Fu, Q., Xu, B., Zheng, Y.C., Yang, Z.S., Hou, Z.Q., Huang, K.X., Liu, Y.C., Zhang, C., Zhao, L., 2017. Two episodes mineralization in the Mengya'a deposit and implication for the evolution and intensity of Pb–Zn–(Ag) mineralization in the Lhasa terrane, Tibet. Ore Geol. Rev. 90, 877–896.

Gao, Y.M., Chen, Y.C., Wang, C.H., Hou, K.J., 2011. Zircon Hf isotopic characteristics and constraints on petrogenesis of Mesozoic-Cenozoic magmatic rocks in Nyainqentanglha region, Tibet. Min. Deposits 30, 279–291 (in Chinese with English abstract).

Gao, S., Luo, T.C., Zhang, B.R., 1998. Chemical composition of the continental crust as revealed by studies in East China. Geochim. Cosmochim. Acta 62, 1959–1975.

Green, T.H., 1995. Significance of Nb/Ta as an indicator of geochemical processes in the crust-mantle system. Chem. Geol. 120, 347–359.

Green, T.H., Pearson, N.J., 1986. Rare-earth element partitioning between titanite and coexisting silicate liquid at high pressure and temperature. Chem. Geol. 55, 105–119.

Griffin, W., Pearson, N., Belousova, E., Jackson, S., Van Achterbergh, E., O'Reilly, S.Y., Shee, S., 2000. The Hf isotope composition of cratonic mantle: LAM–MC–ICPMS analysis of zircon megacrysts in kimberlites. Geochim. Cosmochim. Acta 64, 133–147.

Grove, T.L., Donnelly-Nolan, J.M., Housh, T., 1997. Magmatic processes that generated the rhyolite of Glass Mountain, Medicine Lake volcano, N. California. Contrib. Mineral. Petrol. 127, 205–223.

Guynn, J.H., Kapp, P., Pullen, A., Heizler, M., Gehrels, G., Ding, L., 2006. Tibetan basement rocks near Amdo reveal "missing" Mesozoic tectonism along the Bangong suture, central Tibet. Geology 34, 505–508.

Hanson, G.N., 1978. The application of trace elements to the petrogenesis of igneous rocks of granitic composition. Earth Planet. Sci. Lett. 38, 26–43.

Harris, N.B.W., Xu, R., Lewis, C.L., Hawkeworth, C.J., Zhang, Y., 1988. Isotope geochemistry of the 1985 Tibet Geotraverse, Lhasa to Golmud. Philos. Trans. R. Soc. Lond. 327, 263–285.

Hedenquist, J.W., Lowenstern, J.B., 1994. The role of magmas in the formation of hydrothermal ore deposits. Nature 370, 519–527.

Hofmann, A.W., 1988. Chemical differentiation of the Earth: the relationship between mantle, continental crust, and oceanic crust. Earth Planet. Sci. Lett. 90, 297–314.

Hofmann, A.W., Jochum, K.P., Seufert, M., White, W.M., 1986. Nb and Pb in oceanic basalts: new constraints on mantle evolution. Earth Planet. Sci. Lett. 79, 33–45.

Hoskin, P.W.O., Schaltegger, U., 2003. The composition of zircon and igneous and metamorphic petrogenesis. Rev. Mineral. Geochem. 53, 27–62.

Hou, Z.Q., Cook, N.J., 2009. Metallogenesis of the Tibetan collisional orogen: a review and introduction to the special issue. Ore Geol. Rev. 36, 2–24.

Hou, Z.Q., Qu, X.M., Yang, Z.S., Meng, X.J., Li, Z.Q., Yang, Z.M., Zheng, M.P., Zheng, Y.Y., Nie, F.J., Gao, Y.F., Jiang, S.H., Li, G.M., 2006c. Metallogenesis in the Tibetan collisional orogenic belt: III. Mineralization in the post-collisional extension setting. Miner. Deposits 25, 629–651 (in Chinese with English abstract).

Hou, Z.Q., Yang, Z.S., Xu, W.Y., Mo, X.X., Ding, L., Gao, Y.F., Dong, F.L., Li, G.M., Qu, X.M., Zhao, Z.D., Jiang, S.H., Meng, X.J., Li, Z.Q., Qin, K.Z., Yang, Z.M., 2006a. Metallogenesis in Tibetan collisional orogenic belt: I. Mineralization in main collisional orogenic setting. Miner. Deposits 25, 337–358 (in Chinese with English abstract).

Hou, Z.Q., Pan, G.T., Wang, A.J., Mo, X.X., Tian, S.H., Sun, X.M., Ding, L., Wang, E.Q., Gao, Y.F., Xie, Y.L., Zeng, P.S., Qin, K.Z., Xu, J.F., Qu, X.M., Yang, Z.M., Yang, Z.S., Fei, H.C., Meng, X.J., Li, Z.Q., 2006b. Metallogenesis in Tibetan collisional orogenic belt: II. Mineralization in late-collisional transformation setting. Miner. Deposits 25, 521–543 (in Chinese with English abstract).

Hou, Z.Q., Zheng, Y.C., Yang, Z.M., Rui, Z.Y., Zhao, Z.D., Jiang, S.H., Qu, X.M., Sun, Q.Z., 2013. Contribution of mantle components within juvenile lower-crust to collisional zone porphyry Cu systems in Tibet. Miner. Deposita 48, 173–192.

Hou, Z.Q., Duan, L.F., Lu, Y.J., Zheng, Y.C., Zhu, D.C., Yang, Z.M., Yang, Z.S., Wang, B.D., Pei, Y.R., Zhao, Z.D., McCuaig, T.C., 2015a. Lithospheric architectures of the Lhasa Terrane and its control on ore deposits in Himalayan-Tibetan orogen. Econ. Geol. 110, 1541–1575.

Hou, Z.Q., Yang, Z.M., Lu, Y.J., Kemp, A., Zheng, Y.C., Li, Q.Y., Tang, J.X., Yang, Z.S., Duan, L.F., 2015b. A genetic linkage between subduction- and collision-related porphyry Cu deposits in continental collision zones. Geology 43, 247–250.

Hu, X.M., Garzanti, E., Moore, T., Raffi, I., 2015. Direct stratigraphic dating of India-Asia collision onset at the Selandian (middle Paleocene, 59 ± 1 Ma). Geology 43 (10), 859–862.

Huang, K.X., Zheng, Y.C., Zhang, S., Li, W., Sun, Q.Z., Li, Q.Y., Liang, W., Fu, Q., Hou, Z.Q., 2012. LA-ICP-MS zircon U-Pb dating of two types of porphyry in the Yaguila mining area, Tibet. Acta Petrol. Mineral. 31, 348–360 (in Chinese with English abstract).

Ji, W.Q., Wu, F.Y., Chung, S.L., Li, J.X., Liu, C.Z., 2009. Zricon U-Pb geochronology and Hf isotopic constraints on petrogensis of the Gangdese batholith, southern Tibet. Chem. Geol. 262, 229–245.

Ji, W.Q., Wu, F.Y., Liu, C.Z., Chung, S.L., 2012a. Early Eocene crustal thickening in southern Tibet: new age and geochemical constraints from the Gangdese batholith. J. Asian Earth Sci. 53, 82–95.

Ji, X.H., Yang, Z.S., Yu, Y.S., Shen, J.F., Tian, S.H., Meng, X.J., Li, Z.Q., Liu, Y.C., 2012b. Formation mechanism of magmatic rocks in Narusongduo lead–zinc deposit of Tibet: evidence from magmatic zircon. Miner. Deposits 31, 758–774 (in Chinese with English abstract).

Keller, C.B., Schoene, B., Barboni, M., Samperton, K.M., Husson, J.M., 2015. Volcanic-plutonic parity and the differentiation of the continental crust. Nature 523, 301–307.

Kemp, A.I.S., Hawkesworth, C.J., Foster, G.L., Paterson, B.A., Woodhead, J.D., Hergt, J.M., Gray, C.M., Whitehouse, M.J., 2007. Magmatic and crustal differentiation history of granitic rocks from Hf–O isotopes in zircon. Science 315, 980–983.

Kemp, A.I.S., Hawkesworth, C.J., Collins, W.J., Cray, C.M., Blevin, P.L., 2009. Isotopic evidence for rapid continental growth in an extensional accretionary orogen: the Tasmanides, eastern Australia. Earth Planet. Sci. Lett. 284, 455–466.

Lee, H.Y., Chung, S.L., Wang, Y.B., Zhu, D.C., Yang, J.H., Song, B., Liu, D.Y., Wu, F.Y., 2007. Age, petrogenesis and geological significance of the Lingzizong volcanic successions in the Linzhou basin, southern Tibet: evidence from zircon U-Pb dates and Hf isotopes. Acta Petrol. Sin. 23, 493–500.

Leech, M.L., Singh, S., Jain, A.K., Klemperer, S.L., Manickavasagam, R.M., 2005. The onset of India-Asia continental collision: early, steep subduction required by the timing of UHP metamorphism in the western Himalaya. Earth Planet. Sci. Lett. 234, 83–97.

Li, Y., Audétat, A., 2015. Effects of temperature, silicate melt composition, and oxygen fugacity on the partitioning of V, Mn Co, Ni, Cu, Zn, As, Mo, Ag, Sn, Sb, W, Au, Pb, and Bi between sulfide phases and silicate melt. Geochim. Cosmochim. Acta 162, 25–45.

Li, X.H., Li, Z.X., Li, W.X., Liu, Y., Yuan, C., Wei, G., Qi, C., 2007. U-Pb zircon, geochemical and Sr–Nd–Hf isotopic constraints on age and origin of Jurassic I- and A-type granites from central Guangdong, SE China: a major igneous event in response to foundering of a subducted flat-slab? Lithos 96, 186–204.

Li, J.X., Qin, K.Z., Li, G.M., Xiao, B., Chen, L., Zhao, J.X., 2011. Post-collisional ore-bearing adakitic porphyries from Gangdese porphyry copper belt, southern Tibet: melting of thickened juvenile arc lower crust. Lithos 126, 265–277.

Li, X.F., Wang, C.Z., Mao, W., Xu, Q.H., Liu, Y.H., 2014. The fault-controlled skarn W-Mo polymentallic mineralization during the main India-Eurasia collision: example form Hahaigang deposit of Gangdese metallogenic belt of Tibet. Ore Geol. Rev. 58, 27–40.

Linnen, R.L., Keppler, H., 1997. Columbite solubility in granitic melts: consequences for the enrichment and fractionation of Nb and Ta in the Earth's crust. Contrib. Miner. Petrol. 128, 213–227.

Linnen, R.L., Keppler, H., 2002. Melt composition control of Zr/Hf fractionation in magmatic processes. Geochim. Cosmochim. Acta 66, 3293–3301.

Ludwig, K.R., 2003. In: Isoplot 3.00: A Geochronological Toolkit for Microsoft Excel. Special Publication No. 4. Berkeley Geochronology Center, pp. 1–70.

Ma, W., Yang, Z.S., Hou, Z.Q., Li, Z.Q., Fei, F., Fu, Q., Duan, L.F., Zhao, X.Y., Pei, Y.R., Han, C.H., Liu, Y.C., 2015. Zircon U-Pb dating and the geochemical characteristics of metallogenetic rock from Lietinggang-Leqingla Fe–Cu–Pb–Zn deposit in Tibet. Acta Geol. Sin. 89, 1655–1672 (in Chinese with English abstract).

Mahood, G., Hildreth, W., 1983. Large partition coefficients for trace elements in high-silica rhyolites. Geochim. Cosmochim. Acta 47, 11–30.

Mao, J.W., Zhang, J.D., Pirajno, F., Ishiyama, D., Su, H.M., Guo, C.L., Chen, Y.C., 2011. Porphyry Cu-Au-Mo-epithermal Ag-Pb-Zn-distal hydrothermal Au deposits in the Dexing area, Jiangxi province, East China-A linked ore system. Ore Geol. Rev. 43, 203–216.

Meinert, L.D., 1992. Skarns and skarn deposits. Geosci. Can. 19, 145–162.

Mo, X.X., Dong, G.C., Zhao, Z.D., Guo, T.Y., Wang, L.L., Chen, T., 2005. Timing of magma mixing in the Gangdisê magmatic belt during the India-Asia collision, Zircon SHRIMP U-Pb dating. Acta Geol. Sin. 79, 66–76.

Mo, X.X., Hou, Z.Q., Niu, Y.L., Dong, G.C., Qu, X.M., Zhao, Z.D., Yang, Z.M., 2007. Mantle contributions to crustal thickening during continental collision, evidence from Cenozoic igneous rocks in southern Tibet. Lithos 96, 225–242.

Montel, J.M., Mouchel, R., Pichavant, M., 1988. High apatite solubility in peraluminous melts. Terra Cognita 8, 71.

Mungall, J.E., Brenan, J.M., 2014. Partitioning of platinum-group elements and Au between sulfide liquid and basalt and the origins of mantle-crust fractionation of the chalcophile elements. Geochim. Cosmochim. Acta 125, 265–289.

Pan, G.T., Ding, J., Yao, D.S., Wang, L.Q., 2004. Guidebook of 1: 1500000 geologic map of the Qinghai-Xizang (Tibet) plateau and adjacent areas. Cartogr. Publ. House 1–148 (in Chinese).

Pan, G.T., Mo, X.X., Hou, Z.Q., Zhu, D.C., Wang, L.Q., Li, G.M., Zhao, Z.D., Geng, Q.R., Liao, Z.L., 2006. Spatial-temporal framework of the Gangdese Orogenic Belt and its evolution. Acta Petrol. Sin. 22, 521–533 (in Chinese with English abstract).

Pan, G.T., Wang, L.Q., Li, R.S., Yuan, S.H., Ji, W.H., Yin, F.G., Zhang, W.P., Wang, B.D., 2012. Tectonic evolution of the Qinghai-Tibet Plateau. J. Asian Earth Sci. 53, 3–14.

Petford, N., Atherton, M., 1996. Na-rich partial melts from newly underplated basaltic crust: the Cordillera Blanca Batholith, Peru. J. Petrol. 37, 1491–1521.

Pfänder, J.A., Münker, C., Stracke, A., Mezger, K., 2007. Nb/Ta and Zr/Hf in ocean island

basalts-implications for crust-mantle differentiation and the fate of Niobium. Earth Planet. Sci. Lett. 254, 158–172.

Prouteau, G., Scaillet, B., Pichavant, M., Maury, R.C., 1999. Fluid-present melting of oceanic crust in subduction zones. Geology 27, 1111–1114.

Qiu, J.T., Yu, X.Q., Santosh, M., Zhang, D.H., Chen, S.Q., Li, P.J., 2013. Geochronology and magmatic oxygen fugacity of the Tongcun molybdenum deposit, northwest Zhejiang, SE China. Miner. Deposita 48, 545–556.

Richards, J.P., 2009. Postsubduction porphyry Cu–Au and epithermal Au deposits: products of remelting of subduction-modified lithosphere. Geology 37, 247–250.

Richards, J.P., 2011. Magmatic to hydrothermal metal fluxes in convergent and collided margins. Ore Geol. Rev. 40, 1–26.

Richards, J.P., Kerrich, R., 2007. Special paper: adakite-like rocks: their diverse origins and questionable role in metallogenesis. Econ. Geol. 102, 537–576.

Rickwood, P.C., 1989. Boundary lines within petrologic diagrams which use oxides of major and minor elements. Lithos 22, 247–263.

Rollinson, H.R., 1993. Using Geochemical Data: Evaluation, Presentation. Interpretation. Longman Scientific & Technical, London, pp. 1–352.

Rushmer, T., 2001. Volume change during partial melting reactions: implications for melt extraction, melt geochemistry and crustal rheology. Tectonophysics 342, 389–405.

Sillitoe, R.H., 1989. Gold deposits in western Pacific island arcs: the magmatic connection. Econ. Geol. Monogr. 6, 274–291.

Sillitoe, R.H., 2010. Porphyry copper systems. Econ. Geol. 105, 3–41.

Sisson, T.W., Ratajeski, K., Hankins, W.B., Glazner, A.F., 2005. Voluminous granitic magmas from common basaltic sources. Contrib. Miner. Petrol. 148, 635–661.

Smoliar, M.I., Walker, R.J., Morgan, J.W., 1996. Re–Os ages of group IIA, IIIA, IVA, and IVB iron meteorites. Science 271, 1099.

Stanton, R.L., 1994. Ore elements in arc lavas. Oxford Monogr. Geol. Geophys. 29, 391.

Stepanov, A.S., Hermann, J., 2013. Fractionation of Nb and Ta by biotite and phengite: implications for the "missing Nb paradox". Geology 41, 303–306.

Sun, S.S., Mcdonough, W.F., 1989. Chemical and isotopic systematics of oceanic basalts: implications for mantle composition and processes. Geol. Soc. London Spec. Publ. 42, 313–345.

Titley, S.R., Beane, R.E., 1981. Porphyry copper deposits. Part I: geologic settings, petrology, and tectonogenesis. Econ. Geol. 214–235 75th Anniversary Volume.

Trail, D., Watson, E.B., Tailby, N.D., 2011. The oxidation state of Hadean magmas and implications for early Earth's atmosphere. Nature 480, 79–82.

Wang, R., Richards, J.P., Hou, Z.Q., Yang, Z.M., 2014a. Extent of underthrusting of the Indian plate beneath Tibet controlled the distribution of Miocene porphyry Cu–Mo ± Au deposits. Miner. Deposita 49, 165–173.

Wang, R., Richards, J.P., Hou, Z.Q., Yang, Z.M., DuFrane, S.A., 2014b. Increased magmatic water content–the key to Oligo-Miocene porphyry Cu–Mo ± Au formation in the eastern Gangdese belt, Tibet. Econ. Geol. 195, 1315–1339.

Wang, R., Richards, J.P., Hou, Z.Q., Yang, Z.M., Gou, Z.B., DuFrane, S.A., 2014c. Increasing magmatic oxidation state from paleocene to miocene in the eastern Gangdese Belt, Tibet: implication for collision-related porphyry Cu–Mo ± Au mineralization. Econ. Geol. 1097, 1943–1965.

Wang, R., Richards, J.P., Zhou, L.M., Hou, Z.Q., Stern, R.A., Creaser, R.A., Zhu, J.J., 2015. The role of Indian and Tibetan lithosphere in spatial distribution of Cenozoic magmatism and porphyry Cu–Mo deposits in the Gangdese belt, southern Tibet. Earth Sci. Rev. 150, 68–94.

Wang, R., Weinberg, R.F., Collins, W.J., Richards, J.P., Zhu, D.C., 2018. Origin of post-collisional magmas and formation of porphyry Cu deposits in southern Tibet. Earth Sci. Rev. 181, 122–143.

Wang, Q., Wyman, D.A., Xu, J.F., Dong, Y.H., Vasconcelos, P.M., Pearson, N., Wan, Y.S., Dong, H., Li, C.F., Yu, Y.S., Zhu, T.X., Feng, X.T., Zhang, Q.Y., Zi, F., Chu, Z.Y., 2008. Eocene melting of subducting continental crust and early uplifting of central Tibet: evidence from central-western Qiangtang high-K calc-alkaline andesites, dacites and rhyolites. Earth Planet. Sci. Lett. 272, 158–171.

Wang, B.D., Xu, J.F., Chen, J.L., Zhang, X.G., Wang, L.Q., Xia, B.B., 2010. Petrogenesis and geochronology of the ore-bearing porphyritic rocks in Tangbula porphyry molybdenum–copper deposit in the eastern segment of the Gangdese metallogenic belt. Acta Petrol. Sin. 26, 1820–1832 (in Chinese with English abstract).

Watson, E.B., Wark, D.A., Thomas, J.B., 2006. Crystallization thermometers for zircon and rutile. Contrib. Miner. Petrol. 151, 413–433.

Wedepohl, K.H., 1995. The composition of the continental crust. Geochim. Cosmochim. Acta 59, 1217–1232.

Wen, D.R., Chung, S.L., Song, B., Iizuka, Y., Yang, H.J., Ji, J.Q., Liu, D.Y., Gallet, S., 2008. Late Cretaceous Gangdese intrusions of adakitic geochemical characteristics, SE Tibet, petrogenesis and tectonic implications. Lithos 105, 1–11.

Whalen, J.B., Currie, K.L., Chappell, B.W., 1987. A-type granites: geochemical characteristics, discrimination and petrogenesis. Contrib. Miner. Petrol. 95, 407–419.

Wiedenbeck, M., Allé, P., Corfu, F., Griffin, W.L., Meier, M., Oberli, F., Vonquadt, A., Roddick, J.C., Spiegel, W., 1995. Three natural zircon standards for U-Th–Pb, Lu–Hf, trace element and REE analyses. Geostand. Newslett. 19, 1–23.

Wilson, M., 2001. Igneous Petrogenesis. Kluwer Academic Publishers, London.

Woodhead, J., Hergt, J., Shelley, M., Eggins, S., Kemp, R., 2004. Zircon Hf isotope analysis with an excimer laser, depth profiling, ablation of complex geometries, and concomitant age estimation. Chem. Geol. 209, 121–135.

Wu, F.Y., Jahn, B.M., Wilde, S.A., Lo, C.H., Yui, T.F., Lin, Q., Ge, W.C., Sun, D.Y., 2003a. Highly fractionated I-type granites in NE China (I): geochronology and petrogenesis. Lithos 66, 241–273.

Wu, F.Y., Yang, Y.H., Xie, L.W., Yang, J.H., Xu, P., 2006. Hf isotopic compositions of the standard zircons and baddeleyites used in U-Pb geochronology. Chem. Geol. 234, 105–126.

Wu, Z.H., Ye, P.S., Hu, D.G., Liu, Q.S., 2003b. Thrust system of the north Lhasa block. Geol. Rev. 49, 74–80 (in Chinese with English abstract).

Xu, B., Griffin, W.L., Xiong, Q., Hou, Z.Q., O'Reilly, S.Y., Guo, Z., Pearson, N.J., Gréau, Y., Yang, Z.M., Zheng, Y.C., 2017. Ultrapotassic rocks and xenoliths from South Tibet: contrasting styles of interaction between lithospheric mantle and asthenosphere during continental collision. Geology 45 (1), 51–54.

Yang, Z.M., Lu, Y.J., Hou, Z.Q., Chang, Z.S., 2015. High-Mg diorite from Qulong in southern Tibet: implications for the genesis of adakite-like intrusions and associated porphyry Cu deposits in collisional orogens. J. Petrol. 56, 227–254.

Yang, Z.M., Goldfarb, R., Chang, Z.S., 2016. Generation of postcollisional porphyry copper deposits in southern Tibet triggered by subduction of the Indian continental plate. Soc. Econ. Geol. Spec. Publ.cation 19, 279–300.

Yin, A., Harrison, T.M., 2000. Geologic evolution of the Himalayan-Tibetan orogen. Annu. Rev. Earth Planet. Sci. 28, 211–280.

Yurimoto, H., Duke, E.F., Papike, J.J., Shearer, C.K., 1990. Are discontinuous chondritenormalized REE patterns in pegmatitic granite systems the results of monazite fractionation? Geochim. Cosmochim. Acta 54, 2141–2145.

Zhang, Z.M., Dong, X., Santosh, M., Zhao, G.C., 2014. Metamorphism and tectonic evolution of the Lhasa terrane, central Tibet. Gondwana Res. 25, 170–189.

Zhao, Z.D., Mo, X.X., Nomade, S., Renne, P.R., Zhou, S., Dong, G.C., Wang, L.L., Zhu, D.C., Liao, Z.L., 2006. Post-collisional ultrapotassic rocks in Lhasa Block, Tibetan Plateau: spatial and temporal distribution and its' implication. Acta Petrol. Sin. 22, 787–794.

Zhao, J.X., Qin, K.Z., Li, G.M., Li, J.X., Xiao, B., Chen, L., Yang, Y.H., Li, C., Liu, Y.S., 2014. Collision-related genesis of the Sharang porphyry molybdenum deposit, Tibet: evidence from zircon U-Pb ages, Re–Os ages and Lu–Hf isotopes. Ore Geol. Rev. 56, 312–326.

Zhao, X.Y., Yang, Z.S., Zheng, Y.C., Liu, Y.C., Tian, S.H., Fu, Q., 2015. Geology and genesis of the post-collisional porphyry-skarn deposit at Bangpu, Tibet. Ore Geol. Rev. 70, 486–509.

Zheng, Y.C., Hou, Z.Q., Li, Q.Y., Sun, Q.Z., Liang, W., Fu, Q., Li, W., Huang, K.X., 2012a. Origin of Late Oligocene adakitic intrusives in the southeastern Lhasa terrane, evidence from in situ zircon U-Pb dating, Hf–O isotopes, and whole-rock geochemistry. Lithos 148, 296–311.

Zheng, Y.C., Hou, Z.Q., Li, W., Liang, W., Huang, K.X., Li, Q.Y., Sun, Q.Z., Fu, Q., Zhang, S., 2012b. Petrogenesis and geological implications of the Oligocene Chongmuda-Mingze adakite-like intrusions and their mafic enclaves, southern Tibet. J. Geol. 120, 647–669.

Zheng, Y.C., Hou, Z.Q., Gong, Y.L., Liang, W., Sun, Q.Z., Zhang, S., Fu, Q., Huang, K.X., Li, Q.Y., Li, W., 2014. Petrogenesis of Cretaceous adakite-like intrusions of the Gangdese Plutonic Belt, southern Tibet: implications for mid-ocean ridge subduction and crustal growth. Lithos 190, 240–263.

Zheng, Y.C., Fu, Q., Hou, Z.Q., Yang, Z.S., Huang, K.X., Wu, C.D., Sun, Q.Z., 2015. Metallogeny of the northeastern Gangdese Pb–Zn–Ag–Fe–Mo–W polymetallic belt in the Lhasa terrane, southern Tibet. Ore Geol. Rev. 70, 510–532.

Zheng, Y.C., Hou, Z.Q., Fu, Q., Zhu, D.C., Liang, W., Xu, P.Y., 2016. Mantle inputs to Himalayan anatexis: insights from petrogenesis of the Miocene Langkazi leucogranite and its dioritic enclaves. Lithos 264, 125–140.

Zheng, Y.C., Liu, S.A., Wu, C.D., Griffin, W.L., Li, Z.Q., Xu, B., Yang, Z.M., Hou, Z.Q., O'Reilly, S.Y., 2019. Cu isotopes reveal initial Cu enrichment in sources of giant porphyry deposits in a collisional setting. Geology 47 (2), 135–138.

Zhu, D.C., Zhao, Z.D., Pan, G.T., Lee, H.Y., Kang, Z.Q., Liao, Z.L., Wang, L.Q., Li, G.M., Dong, G.C., Liu, B., 2009. Early Cretaceous subduction-related adakite-like rocks in the Gangdese belt, southern Tibet: products of slab melting and subsequent melt-peridotite interaction. Asian Earth Sci. 34, 298–309.

Zhu, D.C., Zhao, Z.D., Niu, Y.L., Mo, X.X., Chung, S.L., Hou, Z.Q., Wang, L.Q., Wu, F.Y., 2011. The Lhasa Terrane, Record of a microcontinent and its histories of drift and growth. Earth Planet. Sci. Lett. 301, 241–255.

Zhu, D.C., Zhao, Z.D., Niu, Y.L., Wang, Q., Yildirim, D., Dong, G.C., Mo, X.X., 2012. Origin and Paleozoic tectonic evolution of the Lhasa terrane. Geol. J. China Univ. 18, 1–15 (in Chinese with English abstract).

Zhu, D.C., Wang, Q., Zhao, Z.D., Chung, S.L., Cawood, P.A., Niu, Y.L., Liu, S.A., Wu, F.Y., Mo, X.X., 2015. Magmatic record of India-Asia collision. Sci. Rep. 5, 14289.